4-21-2010

Coronal Loop Analysis Using HINODE: EIS and XRT

Lisa Ann Rightmire

To the University Council:

The Thesis Committee for Lisa A. Rightmire certifies that this is the approved version of the following thesis:

Coronal Loop Analysis Using HINODE: EIS and XRT

_____
Joan T. Schmelz, Ph.D., Major Professor

_____
B. N. Narahari Achar, Ph.D.

_____
Donald R. Franceschetti, Ph.D.

Accepted for the Graduate Council:

_____
Karen D. Weddle-West, Ph.D.
Vice Provost for Graduate Programs

STATEMENT OF PERMISSION TO USE

In presenting this thesis in partial fulfillment of the requirements for a Master's degree at The University of Memphis, I agree that the Library shall make it available to borrowers under rules of the Library. Brief quotations from this thesis are allowable without special permission, provided that accurate acknowledgement of the source is made.

Permission for extensive quotation from or reproduction of this thesis may be granted by my major professor, or in [*his/her*] absence, by the Head of Interlibrary Services when, in the opinion of either, the proposed use of the material is for scholarly purposes. Any copying or use of the material in this thesis for financial gain shall not be allowed without my written permission.

Signature_____

Date_____

CORONAL LOOP ANALYSIS USING HINONDE: EIS AND XRT

by

Lisa A. Rightmire

A Thesis

Submitted in Partial Fulfillment of the

Requirements for the Degree of

Master of Science

Major: Physics

The University of Memphis

May 2010

Dedication

I would like to dedicate this Master's Thesis to my son Charles Kai Upton, his father Charles Christopher Upton, and to my mother Linda Ann Bauer. It is their love and support that has given me the drive, determination, and inspiration to pursue this degree. I would also like to thank my advisor Dr. Joan T. Schmelz for sharing her love of sun and her strength as a scientist. Her guidance and encouragement has led me to continue on a path to a career in solar physics. Finally, I would like to thank the entire Physics Department at the University of Memphis. The professors, staff, and students have made Manning Hall a home to me as well as a place of laughs, challenges, and accomplishment.

ABSTRACT

Rightmire, Lisa A. M.S. in Physics. The University of Memphis. May 2010. Coronal Loop Analysis Using HINODE: EIS and XRT. Major Professor: Dr. Joan T. Schmelz.

The goal of this project is to analyze two loops, observed on 2007 December 9, to determine their thermal and density properties. Data were obtained using the EUV Imaging Spectrometer (EIS) and X-Ray Telescope (XRT) instruments onboard HINODE. Atomic physics data was obtained from the CHIANTI database. For the thermal analysis of Loop 1, observed intensities were used to create differential emission measure curves to best fit the data. Density analysis was done using intensity ratios of density-sensitive lines. Results indicate that plasma in Loop 1 is multithermal. Loop 2 was found to exhibit a structure that has yet to be reported in coronal loop literature. The structure appears to be a very hot core with surrounding plasma that cools systematically as distance from the core increases. Solar physics research at the University of Memphis is supported by NSF ATM-0402729 and NASA NNG05GE68G.

TABLE OF CONTENTS

LIST OF TABLES

LIST OF FIGURES

1. Introduction to the Sun

The Sun provides Earth with warmth, light, and the energy that fuels our entire ecosystem. The Sun is the focal point of our solar system. As the largest body in the solar system, it guides the planets in their orbits. It is no surprise that it has been worshiped by cultures throughout history, yet there is still so much that is not known about the Sun. For these reasons, the Sun is an exciting and challenging area of study for the amateur and the professional alike.

Currently, NASA lists four big questions[1] in the field of solar physics: (1) Missing Neutrinos, (2) Origins of the Sunspot Cycle, (3) Nature of Solar Flares, and (4) Coronal Heating Process. By the end of this chapter, the reader should gain an understanding of the nature of each these questions. This chapter will begin by reviewing some of the first discoveries made about the Sun. It will then discuss the Sun in the context of being a stellar body. The methods and instruments used to study the Sun will be outlined. Finally, it will present the Sun, layer by layer, as it is understood today.

1.1 **A Brief History of the Sun**

When talking about the Sun, we don't talk about when it was discovered – the Sun predates human civilization, all life on Earth, and even the Earth itself. Once thought to be constant and unchanging, it has only recently become evident that the Sun is in fact extremely dynamic. Table 1 represents a timeline of the key solar observations that led up to the last one hundred years. Since then, knowledge of the Sun has grown at an extraordinary rate. Each discovery brings new ideas and often conflict. Even now, our understanding of the Sun is constantly being redefined as each new discovery is made.

[1] http://solarscience.msfc.nasa.gov/quests.shtml

Table 1: *A Timeline of the Sun (As outlined by* http://www.hao.ucar.edu/education/spTimeline.php)

Date	Solar Event
1223 BC	The oldest eclipse on record
800 BC	First sunspot observed (possibly)
200 BC	Aristarchus attempts to determine distance to Sun
968 AD	First recorded observation of the corona
1128 AD	First sunspot drawing
1610 AD	Galileo places sunspots on the surface of the Sun
1644 AD	The Sun as a star
1645-1715 AD	Maunder Minimum
1687 AD	Mass of the Sun
1774-1801 AD	Nature of sunspots
1802 AD	Absorption lines discovered
1817 AD	Solar spectroscopy
1843 AD	Sunspot Cycle
1858-1859 AD	Differential Rotation
1859 AD	First solar flare observed / Chemical composition of the Sun
1860 AD	First CME observed
1908 AD	Magnetic nature of sunspots
1919 AD	Suns magnetic cycle

Perhaps one of the most important discoveries about the Sun was the realization that the Sun is in fact a star. This may not seem intuitive because the Sun appears so much brighter than all of the stars we see in the night sky, however the reason for this difference in brightness is distance. While the Sun is a mere 8 light minutes from the earth, the next closest star is 4.3 light years away. (Kutner, 2003, 20) The majority of the brightest stars are even further, being tens or hundreds of light years away. (Pasachoff, 2000, 514-528) This makes our Sun an essential tool to understanding the processes that go on inside a star. However, first it is important to understand the life cycle of a star.

1.2 A Star's Life

In the middle of the twentieth century a process called nuclear fusion was discovered. While many people at the time saw only a tool of war, astrophysicists saw something else: a mechanism for fueling a star. The process begins with an enormous cloud consisting of hydrogen gas mixed with other trace elements. If the cloud is sufficiently dense, the force of gravity will cause this cloud to contract into a structure known as a proto-star. As the proto-star continues to contract, its temperature rises. If this proto-star has a sufficient mass, it will compress until its temperature becomes hot enough, at least ten million Kelvin (Sparke & Gallagher, 2000, 10), to begin the nuclear fusion of hydrogen. This nuclear fusion is the spark of life for a star.

The Hertzsprung-Russell diagram, shown in Figure 1, best characterizes the majority of a star's life. The H-R diagram was conceived of in 1910 by Enjar Hertzprung and Henry Norris Russell (Kutner, 2004). Separately, both astronomers had the idea to plot the surface temperature of the stars versus their luminosities. Most of a star's lifetime is spent in the region know as the Main Sequence. This is the phase of the star's life where the nuclear fusion of the hydrogen core into helium occurs. The duration of this process is dependant on how much hydrogen is present and how quickly the nuclear fusion progresses. More massive stars contain more hydrogen, however because they are more massive their gravitational contraction is also greater. This increased gravitational contraction results in the star becoming much hotter and thereby an increased rate of nuclear fusion. The net result is that the more massive a star is, the shorter the star's lifetime will be.

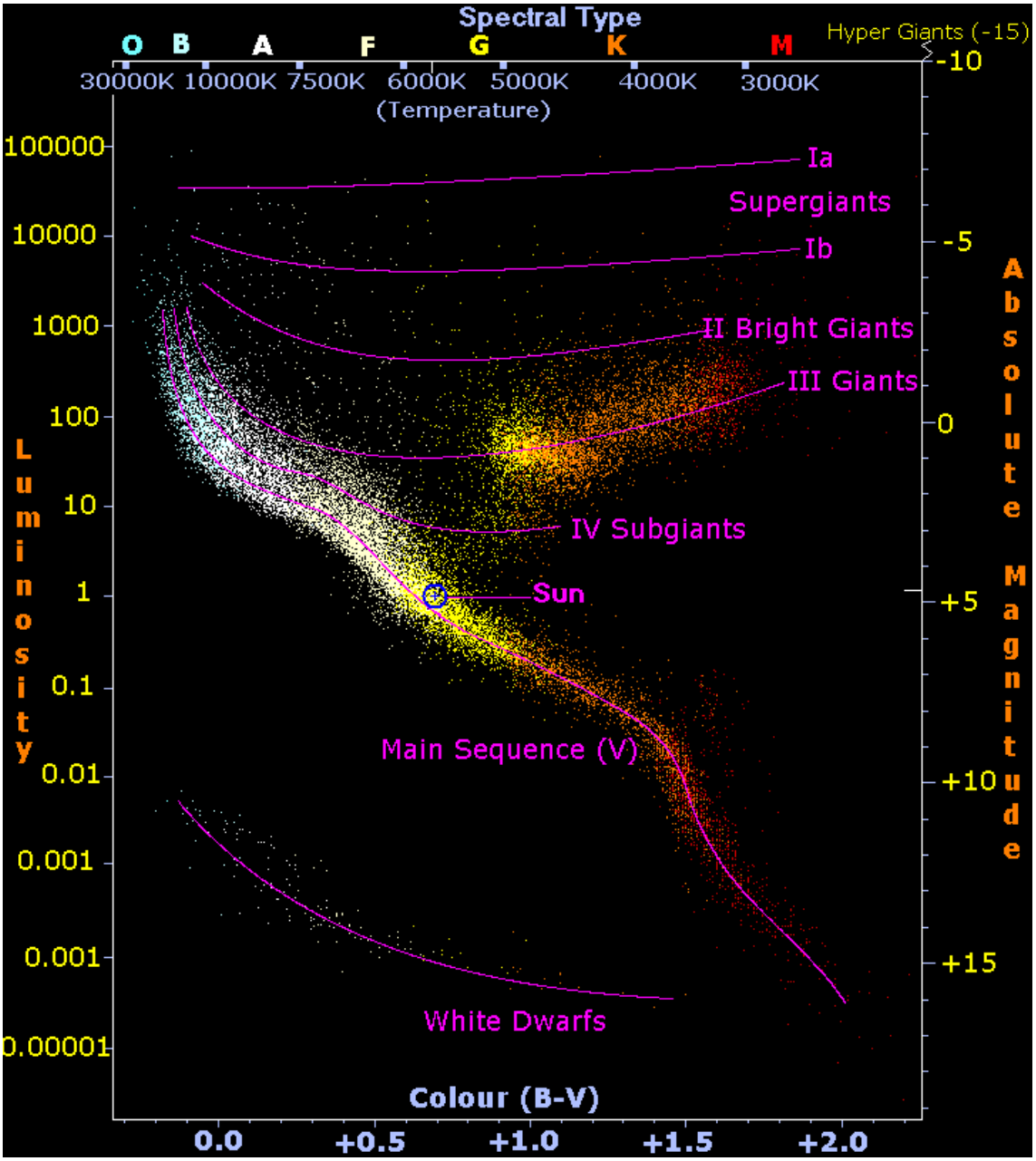

Figure 1: *The Hertzprung-Russell Diagram (Author: Richard Powell, freely liscenced by Creative Commons Attribution ShareAlike 2.5.) This diagram is a plot of stellar temperature vs. luminosity. The hydrogen burning life of the star is spent in the main sequence. Once the hydrogen has been depleted, the star willl expand into a giant or fade into a white dwarf. The Luminosity of a star is related to it's mass and lifetime. Star's in the top left of the main sequence will have masses of 10-60 solar masses and lifetimes on the order of 10^7 years whereas stars on the bottom right will have masses of 0.1-0.3 solar masses and have lifetimes on the order of 10^{12} years.*

The ultimate fate of the star will depend on the star's mass. As the hydrogen in the core of most stars becomes depleted, the core will contract further and the outer layers will expand and cool forming a red giant. During this phase, the contracting core will become hot enough to begin nuclear fusion of the helium. This process occurs very quickly and once complete the outer shells will expand even further. The outer layers then form a planetary nebula surrounding the gradually cooling core, known as a white dwarf. This is what is commonly revered to as a nova. In much larger stars, however, fusion of the core into heavier elements may occur. In these stars, the core will become so massive that it will approach the Chandrasekhar limit[2]. Once this limit has been reached, the core will collapse and the remaining matter will be converted into neutrons. This process causes an explosion known as a supernova, leaving behind a neutron star, or in more extreme cases a black hole may be formed.

Amid the darkness of a dying star, there is light to be found. As with most things in nature, the cycle of life continues. The material that was expelled from a supernova (or nova, in the form a planetary nebula) will create new molecular clouds. Like the stars they were born from, this material in turn will begin to collapse and the next generation of stars will be formed. New stars formed in this way will contain more trace elements. They will be denser, will reach higher temperatures, and will generally have shorter lifetimes, but it is in this way that the galaxy will continue to evolve.

Stars like the Sun, our star, will have an average lifetime of ten billion years. The Sun is currently in the middle of that lifetime. Examining the birth, life and death of a star provide a general overview of where the Sun came from and what a star's ultimate fate

[2] The Chandrasekhar limit is approximately 1.4 solar masses. Once a white dwarf reaches this size, its electrons will approach the speed of light. Since they are unable to travel faster than the speed of light, the white dwarf's gravity will overcome the outward pressure and the white dwarf will collapse.

will be. However, the Sun provides an opportunity to not only understand a broad outline of stellar mechanisms, but to look deeper into the details of the inner workings of a star. These inner workings have proved to be very complex. While the answers for many questions have been found, many unanswered questions still remain. This highlights the importance of not only studying the Sun as it relates to our solar system, but of viewing the Sun as a window into the lives of the billions of other stars in the universe.

1.3 Observing the Sun

How do we study the Sun? The answer lies in the difference between night and day – light! In the late 1600's, Newton discovered that a prism could be used to split visible light into its component colors, producing a rainbow. This rainbow, or spectrum, is actually a plot of the light as a function of wavelength. The study of light that has been split into its spectrum is known as spectroscopy. Spectroscopy has proven to be one of the most valuable techniques for studying the Sun. However, the spectrum of visible light[3] makes up only a tiny portion of the electromagnetic spectrum. The ultraviolet, x-ray, and infrared portions of the spectrum are blocked by the Earth's atmosphere. Early observations of the Sun were therefore limited to the visible portion of the spectrum.

One of the earliest scientists to closely study the visible spectrum was Josef von Fraunhofer. In 1814, he used a prism to create images of the visible spectrum of sunlight and found that several black lines marred the spectrum. These lines, now known as Fraunhofer lines, were found to be caused by the absorption of photons by a cool gas surrounding the hotter light emitting gas (Golub & Pasachoff, 2001). The placement of these lines is dependent on the chemical composition of the surrounding gas. By

[3] Light with wavelengths ranging from about 400nm to 700nm

examining the patterns of the Fraunhofer lines, astronomers have been able to determine the chemical makeup of the Sun, which is composed primarily of hydrogen and helium.

Eclipses occur when the moon's path passes between the Earth and the Sun, causing a shadow on the surface of the Earth. In most cases the moon will block only a portion of the Sun, however if the placement of the Earth, Moon, and Sun is just right, a small portion of the Earth will be able to witness a total solar eclipse. In a total solar eclipse, totality occurs when the moon passes directly in front of the Sun causing the entire Sun, with the exception of the far-reaching corona, to be blocked by the moon. Very little of the Sun's light, about one millionth (Phillips, 1992, 26), is actually produced in the corona, so that when this dramatic event occurs, only the Sun's corona is visible and those in that path of totality will be shrouded in darkness. Solar physicist recognized that totality provided a unique opportunity to observe the corona. By using a spectrograph at the time of totality, the spectrum of the light emitted by the corona could be observed. In fact, it was by this method that helium was first discovered (Golub & Pasachoff, 1997, 46). Eclipses were so effective for studying the corona that they led to the invention of a new instrument called a coronagraph. A coronagraph is essentially a spectrograph that includes an occulting disk, a special disk designed to mimic a solar eclipse. While the coronagraph has become an essential tool for solar physics, eclipses are more effective at occulting the Sun and are still studied by solar physicists (Golub & Pasachoff, 2001). Observatories designed for studying the Sun have been built all over the world. The largest and most well known of the traditional optical observatories that study the Sun include Mount Wilson Observatories, Mauna Loa Solar Observatories[4], Big Bear Solar

[4] Run by High Altitude Observatories

Observatories, Swedish Solar Observatories, Teide Observatories, and the U.S. National Observatories. Table 2 lists these observatories, their telescopes, location, year they were built, and the diameter of the telescope lens. Radio[5] telescopes used to study the Sun include Nancay Radioheliograph in France, Nobeyama Radio Observatory in Japan, and the Very Large Array in NM. In addition to these already active telescopes, two new telescopes are currently being developed. Teide Observatories has already begun construction on the GREGOR Solar Telescope (150cm) in Germany. More impressively is the collaborative effort to build a very large (400cm) solar telescope on Haleakala in Maui. Currently in planning, the Advanced Technology Solar Telescope is expected to begin construction in 2010 and first light is expected to be in 2017. Once complete, the large aperture combined with adaptive optics is expected to provide images of the Sun with a resolution on the order of one tenth of an arc second.

***Table 2**: Ground Based Solar Telescopes*

Observatory Name	Telescope Name	Location	Date Built	Diameter (cm)
Mount Wilson Observatory	Snow Telescope	Mt. Wilson, CA	1903	61
Teide Observatories	Vacuum Tower Telescope	Tenerife, Canary Islands	1989	70
Teide Observatories	THEMIS Solar Telescope	Tenerife, Canary Islands	1996	90
Swedish Solar Observatories	Swedish Solar Telescope	La Palma, Canary Islands	2002	100
National Solar Observatories	Richard P. Dunn Solar Telescope	Sunspot, NM	1969	152.4
Big Bear Observatories	New Solar Telescope	Pasadena, CA	2008	160
National Solar Observatories	McMatth-Pierce Solar Telescope	Kitt Peak, AZ	1961	161
Mauna Loa Solar Observatories	N/A	Haleakala, HI	N/A	N/A

[5] Radio wavelengths emitted by the Sun are also able to penetrate the Earth's atmosphere

In recent years, new methods of studying the Sun have been developed. The nuclear fusion that occurs in the Sun should produce a type of particle know as a neutrino. These particles, the smallest know particles, are extremely hard to detect because primarily they only interact with matter via the weak nuclear force (Golub & Pasachoff, 2001). Experiments designed to take advantage of the most probable neutrino interactions, have been developed to detect neutrinos. The first of these experiments was the Homestake experiment, followed by the Kamiokande, Super-K[6], and BOREXINO experiments. However, these experiments are only able to detect the more uncommon high-energy neutrinos. The SAGE and GALLEX experiments are designed to be able to detect neutrinos created by proton-proton reactions, most commonly produced in the Sun. Up to this point, neutrino detectors were only been able to detect a fraction of the expected number of neutrinos - a discrepancy referred to as the neutrino problem. Finally, the Sudbury Neutrino Observatory was designed to detect all types of neutrinos. They were able to verify that neutrinos could change type, leading to changes in our current understanding of solar physics as well as nuclear physics.

Another recently developed method of studying the Sun is Helioseismology. Seismologists study the movement of waves through various mediums, and likewise Helioseismologists study how waves move inside the Sun, allowing solar physicists to learn about the solar interior. Helioseismology has shown that the waves moving inside the Sun have specific modes of oscillation. Careful analysis of these modes of oscillation can be used to determine how plasma moves inside the Sun. One of the most significant results so far has shown that the motion of the Sun's plasma varies with depth.

[6] Also known as Kamiokande II

1.4 Space Based Instruments

As the technology advanced, astronomers were no longer limited to ground based telescopes - the instruments could now be put into space. Without the interference of the Earth's atmosphere, whole new areas of the spectrum could be observed[7]. With the proper orbital placement, observations were no longer restricted to the day, allowing for observations for extended periods of time. Over the last several decades, many instruments (see Table 3) have been sent into space to study the Sun. These instruments have brought new discoveries as well as new questions.

Space-based study of the Sun began with the development of rockets carrying instruments, launched high into the atmosphere to take measurements. After a short period of observation, these instruments would begin falling back to Earth, where they would be found and if not destroyed in the fall, the data could be analyzed. In the 1960's NASA began launching satellites known as Orbiting Solar Observatories (OSOs) to study UV and X-Ray emissions from orbit. NASA's manned mission, Skylab, was launched in 1973 and a new age of solar observation began. New solar structures were revealed and the true nature of the Sun had begun unfolding. Through most of the1980's, Solar Maximum Mission (SMM) continued to provide details of these newly discovered structures. The Ulysses was launched in 1990 as a collaborative effort between the European Space Agency (ESA) and NASA. It used Jupiter's gravity to slingshot over the solar poles.

[7] The corona, the focus of research at the University of Memphis, is best observed in the extreme ultraviolet (EUV) and x-ray regions of the spectrum.

***Table 3**: The Missions and Instruments*

Year	Missions	Instruments	Focus
1940's	Rockets		Solar Wind
1962-1975	OSO - Orbiting Solar Observatories (1-8)	Imagers	UV, X-Ray
1973	Skylab	Apollo Telescope Mount	UV, X-Ray
1980-1989	SMM - Solar Maximum Mission	UVSP - UV Spectrometer and Polarimeter	UV
		ACRIM - Active Cavity Radiometer Irradiance Monitor	Solar Energy
		GRS - Gamma-Ray Spectrometer	Gamma-Ray
		HXRBS - Hard X-Ray Burst Spectrometer	Hard X-Ray
		XRP - X-Ray Polychomator	Soft X-Ray
		HXIS - Hard X-Ray Imaging Spectrometer	Hard X-Ray
		CP -Coronagraph Polarimeter	Corona
1990	Ulysses	VHM -Vector Helium Magnetometer	Magnetic Fields
		FGM - Fluxgate Magnetometer	Magnetic Fields
		SWOOPS - Solar Wind Observations Over the Poles of the Sun	Solar Wind
		SWICS - Solar Wind Ion Composition Spectrometer	Solar Wind
		URAP - Unified Radio and Plasma	Radio Sources
		EPAC - Energetic PArticles Composition	Energetic Particles
		HI-SCALE - Heliosphere Instrument for Spectra, Composition, and Anisotropy at Low Energies	Interplanetary Ions and Electrons
		COSPIN - COsmic ray and Solar Particle Investigation	Energetic Particles
		GRB - Gamma-Ray Burst	Gamma-Ray
		SCE - Solar Corona Experiment	Solar Atmosphere
		GWE - Gravitational Wave Experiment	Gravity Waves
1992-2001	Yohkoh	SXT - Soft X-Ray Telescope	Soft X-Ray
		HXT - Hard X-ray Telescope	Hard X-Ray
		BCS - Bragg Crystal Spectrometer	X-Ray
		WBS - Wide Band Spectrometer	X-Ray

***Table 3 (cont)**: The Missions and Instruments*

Year	Missions	Instruments	Focus
1995	SOHO -Solar and Heliospheric Observatory	MDI - Michelson Doppler Imager	Helioseismology
		CDS - Coronal Diagnostic Spectrometer	Corona
		EIT - Extreme ultraviolet Imaging Telescope	Corona
		SUMER - Solar Ultraviolet Measurement of Emitted Radiation	Corona
		UVCS - UltraViolet Coronagraph Spectrometer	Corona
		LASCO - Large Angle and Spectrometric Coronagraph	Corona
		SWAN - Solar Wind ANisotropies	Solar Wind
		CELIAS - Charge ELement and Isotope Analysis System	Solar Wind
		COSTEP - Comprehensive SupraThermal and Energetic Particle	Solar Wind
		ERNE - Energetic and Relativistic Nuclei and Electron	Solar Wind
		VIRGO - Variability of solar IRradiance and Gravity Oscillations	Oscillations
		GOLF - Global Oscillations at Low Frequencies	Oscillations
1998	TRACE - Transition Region and Coronal Explorer	UV/EUV Imager	Corona
2002	(R)HESSI - Ramaty High Energy Solar Spectroscopic Imager	High-Energy Solar Spectral Imager	X-Ray, Solar Flares
2007	HINODE	EIS - Extreme UV Imaging Spectrometer	EUV
		XRT - X-Ray Telescope	X-Ray
		SOT - Solar Optical Telescope	Visible
2010	SDO - Solar Dynamics Observatory	EVE - Extreme UV Experiment	EUV
		AIA - Atmospheric Imaging Assembly	UV, EUV
		HMI - Helioseismic and Magnetic Imager	Helioseismology

In the last fifteen to twenty years more sophisticated instruments have been developed and put into space. In 1992 the Japanese launched Yohkoh, which included two x-ray telescopes as well as two spectrometers. SXT was unique in that it was the first soft x-ray telescope to use a charge coupled device (CCD) imager instead of film. The Solar and Heliospheric Observatory (SOHO), another ESA/NASA collaborative effort, was launched in 1995. SOHO houses twelve instruments for studying various aspects of the Sun, such as Helioseismology, the Inner and Outer Corona, and the Solar Wind. SOHO includes CDS (Coronal Diagnostic Spectrometer) and the Extreme ultraviolet Imaging Telescope (EIT) for detecting extreme ultraviolet (EUV) emissions. NASA launched the Transition Region and Coronal Explorer (TRACE) in 1998. The primary goal of TRACE is the study of the lower part of the corona with extremely high resolution. In 2002, NASA launched RHESSI to study the release of energy in solar flares.

Four nations[8] came together with the launch of Hinode in 2006. Hinode currently houses the highest resolution instruments for viewing the Sun in the optical, EUV, and X-Ray wavelengths: the Solar Optical Telescope (SOT), the Extreme UV Imaging Spectrometer (EIS), and the X-Ray Telescope (XRT). However, earlier this year the Solar Dynamics Observatory (SDO) launched. SDO houses three instruments: the Atmospheric Imaging Assembly (AIA), the Extreme Ultraviolet Variability Experiment (EVE), and the Helioseismic and Magnetic Imager (HMI). SDO expects to receive first light in the spring of 2010, and will greatly improve the resolution of images in the UV and EUV wavelengths. With so many instruments providing more information than ever before, now is a very exciting time for solar physicists.

[8] Japan, the United States, Europe, and the United Kingdoms

1.5 The Sun's Many Layers

The Sun can be divided into many layers (shown in Figure 2), each with different properties. The inside of the Sun, known as the solar interior, consists of the core, the radiative zone, and the convective zone. The solar atmosphere begins with the surface of the Sun, the photosphere, and includes the chromosphere, the transition region, and the solar corona. Beyond the solar atmosphere, the solar wind carries high-energy particles far out into solar system. Much of the Sun is still not understood. As knowledge of the Sun grows, a model, known as the standard model, is created to describe the physical processes of the Sun. This model is governed by the facts that have been gathered about the Sun, as well as a principle known as hydrostatic equilibrium. In short, hydrostatic equilibrium means that the outward pressure of each layer of the Sun must be in balance with the gravitational force of the layers above it. (Phillips, 1992, 48) This section provides an overview of the solar interior and the solar atmosphere, as they are believed to exist by the current standard model.

The core is the driving force of the Sun, producing energy via the nuclear fusion of hydrogen into helium. The volatile core, which has been heated by the balance of outward pressure with the gravitation force, reaches a temperature of about fifteen million Kelvin (Phillips, 1992, 51). At this temperature the atoms completely ionized and move at speeds great enough to undergo fusion. The three-step process by which hydrogen fuses into helium is known as the proton-proton chain, shown in Figure 3. To begin this process, a deuteron[9] is formed by the fusion of two protons, i.e. hydrogen nuclei. During this step, a positron and a neutrino are also released. Once created, the

[9] A deuteron is an atom with a single neutron and single proton.

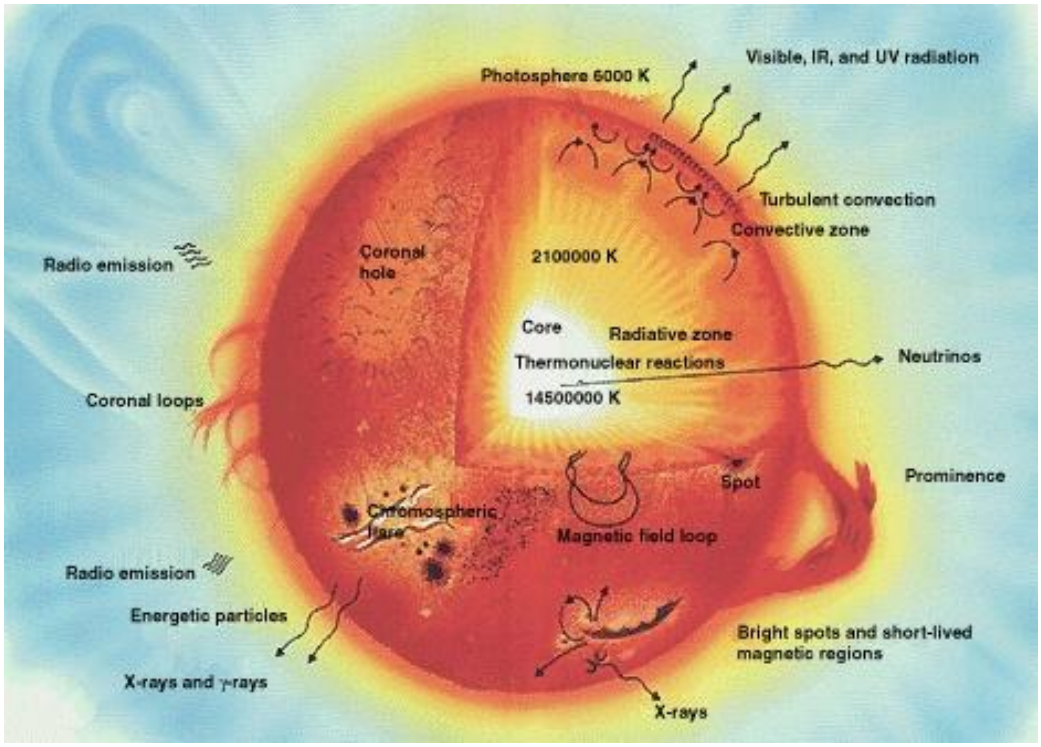

Figure 2: *Diagram of the Sun (Courtesy of NASA's* Imagine the Universe! Website.*) This is a diagram of several layers of the Sun, the emmissions of each layer, and notable features of the Sun.*

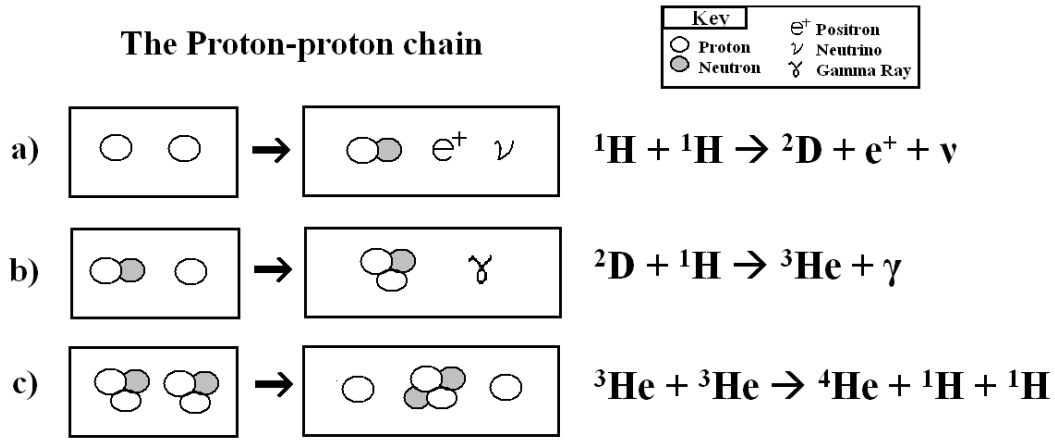

Figure 3: *The Proton-proton Chain. This is a diagram of the reactions that make up the proton-proton chain of reactions, by which helium is produced in the Sun.*
a) Two hydrogen nuclei fuse to produce a deuteron, releasing a positron and a nuetrino in the process. b) A deuteron and a hydrogen nucleus fuse to produce a helium nucleus(with only one nuetron), releasing a gamma-ray in the process. c) Two helium nuclei (each with only one nuetron) fuse to produce a helium nucleus (with two neutrons) and two hydrogen nuclei.

deuteron immediately fuses with a third proton to create a helium nucleus containing only one neutron, releasing a gamma-ray in the process. To complete the proton-proton chain, two helium nuclei, having only one neutron each, fuse to create two hydrogen nuclei and a single helium nucleus, with two neutrons. The result of the entire process is the conversion of mass into energy, which radiates into the next layer in the form of photons.

The region between the core and the surface of the Sun is divided according to how energy is transported outward. As energy leaves the core, it enters a layer known as the radiative zone. Near the core the Sun is very dense and particle interactions, scattering predominantly, occur with a high frequency. These interactions essentially trap the photons as they bounce around, slowly trying to find a path leading outwards. As they progress further from the core, the temperature and density drop dramatically. As the photons arrive in the region know as the convection zone, the temperature reaches one million Kelvin (Phillips, 1992, 51). Inside this region, the gas is cool enough to support atoms with intact electrons. These atoms are cycled by convection, continually rising and falling, and absorb many of the photons entering the convection zone. From the time it was created in the core, it takes a photon 100,000 years (Golub, & Pasachoff, 2001, 51) to pass through the radiation zone and convection zone and finally reach the surface of the Sun.

The surface of the Sun is known as the photosphere. It was given this name because this is the region of the Sun that produces the visible light that is able to pass through the earth's atmosphere to the surface. In order to emit light at this wavelength, the temperature of the surface of the Sun must be approximately 6000 K[10]. The first

[10] This was later confirmed to be 5778 K (Phillips, 1992,83-84).

feature of the photosphere, as well as the Sun, to be observed was the sunspot. Sunspots, dark regions appearing on the surface of the Sun, are formed when the magnetic field lines pass through the photosphere, preventing or redirecting photon emission. A recently discovered feature of the photosphere is granulation[11]. This effect is thought to be due to the "bubbling up" of convection currents on the surface of the Sun.

The region of the Sun above the photosphere is called the chromosphere. The chromosphere takes its name from its red appearance during an eclipse. This region of the Sun is said to be "optically thin" because the light that it emits is too faint to be seen with the bright photosphere underneath. It is best viewed during an eclipse when the moon blocks the light from the photosphere, however special filters designed for viewing hydrogen alpha emissions, can be used as well. With a temperature of 10,000-15,000 K, the chromosphere appears to be made up of a feature know as spicules. The name comes from the fact that when viewed from the side, these features appear to be clusters of small spikes. The chromosphere also features granules, known as supergranules, which are about thirty times larger than those found in the photosphere.

The outer most layer of the Sun is the corona. The far-reaching corona is perhaps the most mysterious region of the Sun. Between the chromosphere and the corona the temperature quickly rises to two million Kelvin, in a very thin layer aptly named the transition region. The mechanism for this rapid increase in temperature is unknown and is commonly referred to as the coronal heating problem[12]. At these temperatures, most of the light emitted from the corona is in the X-ray or EUV portion of the spectrum. In addition to extreme temperatures, a very low density characterizes the solar corona.

[11] Only recently discovered because they require instruments with a resolution of about one arcsec.

[12] This is the primary motivation for the work in this Master's Thesis.

These densities are so low that there is no clear outer edge to the corona. Instead of an outer edge, the corona gradually tapers of into a stream of outward moving particles known as the solar wind. Two types of solar wind have been discovered. The faster of the two types appears from regions know as coronal hole, whereas the slower of the two types radiates from all other regions of the corona. Coronal holes are regions of the corona where the Suns magnetic field extends deep into space, rather that looping back into the Sun. These extended field lines act like roadways, allowing the solar wind to travel at much greater speeds. In areas where the magnetic field lines loop back into the Sun, beautiful structures know as coronal loops are formed. In these structures, plasma rises out of the Sun and is funneled through the magnetic field lines back into the Sun, creating shapes that appear like enormous arches. Bright eruptions know as solar flares can also be observed. The exact cause of these solar flares is not known, however it is thought that they may occur when the magnetic field lines well up from the surface of the Sun, break, and then reconnect. It is thought that the eruption is due to a release of energy, stored in the magnetic field, as the field lines break. Finally, the most violent feature to be observed in the corona is known as a corona mass ejection (CME). CMEs occur when giant clumps of the corona break away from the Sun, creating eruptions that are several times the size of the Sun itself.

1.6 The Solar Activity Cycle

Many solar processes are fairly consistent and ongoing. These types of processes are referred to as being elements of the quiet Sun. However features such as sunspots, solar flares, filaments, prominences, coronal loops and coronal mass ejections are

referred to as being elements of the active Sun. The frequency of these events fluctuates over time. By observing the number of sunspots in the middle 1800s, Samuel Heinrich Schwabe was the first astronomer to observe that appearance of sunspots was cyclic, with a period averaging about 11 years. As new features of the Sun were discovered, it was found that the other features of the active Sun varied along with sunspot activity. For this reason, sunspots are now commonly accepted as a measure of solar activity.

Solar activity has been attributed to disruption of satellite function, electrical systems, and Earth's climate. Solar flares and coronal mass ejections send a large amount of charged particles into space. As they approach the Earth, most of these particles are redirected to the poles by Earth's magnetic field. When the high-energy particles enter the atmosphere, plasma is created and the phenomena known as the auroras can be seen. When large solar flares or coronal mass ejections are directed towards the Earth, the solar wind has enough energy to disrupt the Earth's magnetic field, causing geomagnetic storms. When this occurs, the charged particles can damage satellites that are in orbit and disrupt communications. If enough charged particles reach the Earth's surface, entire power grids can be knocked offline, such as the case of the Hydro-Quebec power grid in March 1989. The impact of the solar cycle on Earth has created a need for methods to predict sunspot activity[13].

In 1848, astronomer Johann Rudolph Wolf created the method for calculating the relative sunspot number[14] (R_z). The relative sunspot number is calculated by counting the number of sunspot groups as well as the number of individual sunspots observed. The number of groups is multiplied by ten and then added to the number of sunspots. This

[13] This need is becoming more evident as space travel becomes more commonplace.

[14] Also know as the International Sunspot Number.

number is then multiplied by a corrective factor to get the relative sunspot number. Wolf later became director of the Zurich Observatory, which kept a record of this count until 1981. From 1874 to 1976, the Royal Greenwich Observatory not only kept records of sunspot numbers, but also of their positions and size. Since 1976, the US National Oceanic and Atmospheric Administration (NOAA) has maintained the sunspot record.

Scientists that observe fluctuations in sunspot activity have discovered characteristics of the sunspot cycle, such as differential rotation, polarity, and the butterfly effect. In the middle of the 1800's, an astronomer by the name of Richard Carrington studied the motion of sunspots. He found that sunspots near the equator were faster than those further from the equator. This variation in the rotation rate of the Sun is known as differential rotation. Differential rotation causes the Sun's magnetic field lines to wrap around the equator. Scientists observing the magnetic polarity of the sunspots have found that the polarity of the sunspots, as well as the Sun's magnetic field, will reverse from one cycle to the next. Finally, the latitude and total area of sunspots increases as the sunspot cycle progresses. When this information is plotted out, as shown in Figure 4, a repeating butterfly-like image is created[15]. While we are beginning to understand the characteristics of the solar cycle, the underlying mechanism behind what causes fluctuations in the solar cycle has yet to be determined[16].

[15] Notice that larger, brighter "butterflies" correspond to more active solar cycles.

[16] Leading theories are based on the transport of magnetic flux near the surface of the Sun.

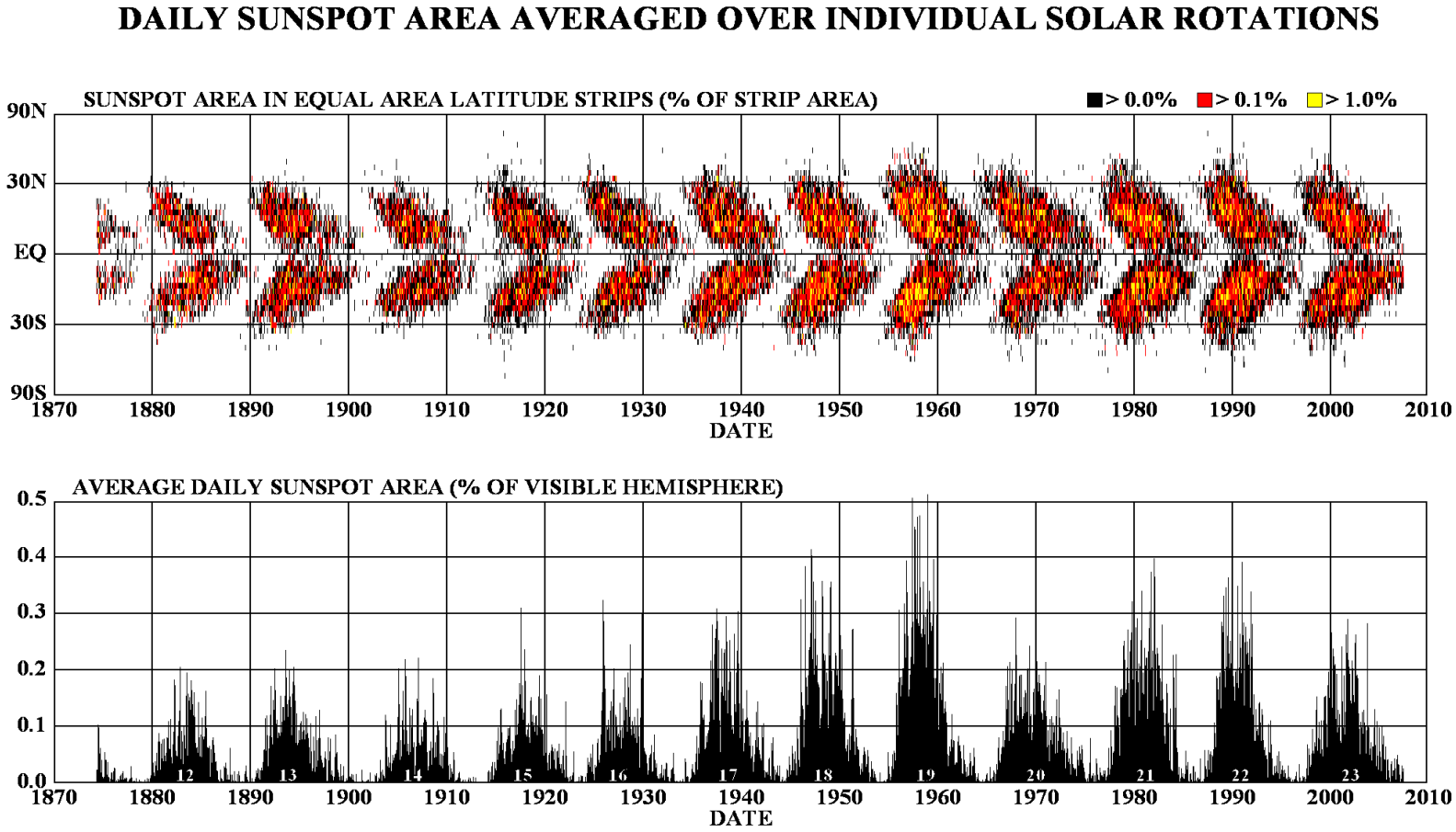

Figure 4: *Butterfly Diagram. (Courtesy of NASA.) This image shows how the latitude (vertical position) and total area (color coded) of sunspots as changed over time. A repeating butterfly-like image is formed, where brighter "butterflies" correspond to more active solar cycles.*

2. Motivation for Research

The search for a complete understanding of the Sun is ongoing. While great strides are being made, there is still a long road ahead. The physics behind the Sun has proven to be more robust that perhaps anyone ever thought it could be. When embarking on a journey of this order of magnitude, it is important to remember the driving force: the joy of unraveling the mysteries of the universe and finding the beauty in the delicately woven science that brings it all together and makes it all possible.

One of the biggest mysteries in solar physics is the mechanism behind coronal heating. The surface of the Sun reaches temperature of nearly 6000K. However, it has been found that the temperature of the corona is on the order of 1-2MK. The temperature is expected to decrease as the distance from the center of the Sun increases. Since there is a massive increase of temperature in the corona, some unknown heating mechanism must exist. The question then becomes: What process is the driving force behind this heating? The solution lies buried deeply in the structure of coronal loops. The method of solving this mystery has been clearly outlined: 1) Determine the temperature profile for coronal loops and 2) Use this knowledge to find a heating model. However, like the plasma being funneled through the magnetic fields, the answers are often fleeting. Solutions seem to appear, rising out of the surface but then dissipate into unknown just as quickly as they were formed. With only observations of something occurring millions of miles away, the explanation might seem elusive or intangible. However, the search requires persistence if it is ever to be realized. The goal of this chapter is to outline the evolution of the search thus far, determine what has been learned, and apply this knowledge to continuing the quest for the answers.

2.1 Finding a Heating Mechanism

The corona is best observed in the EUV and x-ray regions of the spectrum. Skylab, launched in 1973, was one of the first missions to begin studying these regions of the Sun's spectrum. Rosner, Tucker, and Vaiana examined Skylab observations (Rosner et al. 1978.) and used them as a basis to create a coronal loop model in order to determine loop characteristics. The loops they examined were hot X-ray loops[1] that were somewhat stable and thus they assumed hydrostatic equilibrium for the life of the loop. Based on this assumption, they created a loop model by balancing the energies and forces that are involved[2]. From this energy relation

$$E_H + \boldsymbol{f}\cdot\mathbf{v} = \text{div}\,\mathbf{F}_c - E_R + \text{div}\,(\{1/2\,\rho v^2 + U\}\mathbf{v} + \rho\mathbf{v}), \qquad (1)$$

they developed an energy relation for the entire loop:

$$\int_v (E_H + \boldsymbol{f}\cdot\mathbf{v})d^3r = -\int_v E_R d^3r + L_{footpoint} + L_{sides}. \qquad (2)$$

From further examination of this relation, they determined that the maximum loop temperature (T_{Max}) occurs when radiative losses balance with the energy deposition such that the conductive flux is negligible. This implied that in order to maintain equilibrium, T_{Max} must be located at the top of the loop. They conclude that in order to maintain this condition, heating must occur over the majority of the loop length. Furthermore, they concluded that loop temperature and pressure are based on loop size but are modulated by the heating function.

As the turn of the millennium approached, new instruments had been launched and as the results were coming in, the question of coronal heating resurfaced in an issue

[1] Hot loops correspond to X-ray emissions and cool loops correspond to EUV emissions.

[2] The energy relation (Rosner et al.1978) is supposed to balance: local mechanical heating function (E_H), volume force ($\boldsymbol{f}$) due to gravity or the heating mechanism, plasma velocity ($\mathbf{v}$), radiative loss (E_R), and conductive losses or gains through the surfaces of the loop ($L_{footpoint} + L_{sides}$.).

of Nature magazine. Priest et al. (1998) examined a coronal loop observed with SXT and obtained a temperature profile that showed an increase in temperature moving towards the top of the loop. They then outlined three fundamental heating models: footpoint, summit, and uniform heating. They compared these models with the SXT observations and determined that the uniform heating model provided the best fit. They go on to suggest that in order to solve the mystery of coronal heating, future analysis should be done by using "observed temperature profiles to deduce the form of heating in coronal loops and arcades and secondly to use that heating form to deduce the likely heating mechanism."

2.2 The Debate Heats Up

Aschwanden et al. (1999) created a method called "dynamic stereoscopy" in order to determine the precise geometry of an arcade of loops that was observed by EIT. The goal of this complex analysis was to isolate individual loops or loop segments so that their precise characteristics could be determined. They isolated thirty loops and then used an EIT 171/195 Å filter ratio method to determine the temperature profiles of those loops[3]. The filter ratio analyses produced results that indicated an isothermal loop temperature around 1.2MK. They then used the energy relations outlined by Rosner et al. (1978) to determine that radiative cooling was significantly larger than conductive cooling and therefore these loops could not be in a steady state. However, when they combined their temperature and density profiles, they concluded that the analyzed loops

[3] It is important to note that this method assumes that the loop density is constant and loop temperature is isothermal through the line of sight.

were in hydrostatic equilibrium. All together their results indicated that a footpoint heating mechanism was at work.

Lenz et al. (1999) analyzed four regions spaced across four different TRACE loops. The 171 Å filter was used to create density profiles and the 171/195 Å filter ratio method was used to determine loop temperature profiles. They determined that the temperatures were essentially isothermal along the length of each loop. They go on to suggest that the isothermal temperature profiles resulting from EIT and TRACE EUV observations may indicate the existence of a class of loops with different characteristics than those that had been previously observed with X-ray instruments.

Schmelz et al. (2001) examined thirteen pixels on a loop observed with CDS. The initial temperature analysis was done by comparing the intensity ratios of iron lines to the ratio of their contribution functions, G(T):

$$(I_{346} / I_{353}) = (353/346)[G_{346}(T) / G_{353}(T)]. \qquad (3)$$

These ratios produced multiple temperatures for each pixel on the loop, indicating that the loop plasma could not be isothermal through the line of sight (LOS.) They incorporated SXT observations of the same loop in order to extend the range of their temperature analysis. Rather than using the filter ratio method, they allowed for a multithermal plasma by creating a differential emission measure (DEM) function such that:

$$I_\lambda = (1/4\pi)\,(hc/\lambda)\,A \int G(T)\,DEM(T)\,dT, \qquad (4)$$

where A is the elemental abundance given by the CHIANTI atomic physics database. They then used forward folding[4] to create the loop temperature profiles. The temperature profiles they obtained varied over the length of the loop and had peak temperatures that were much larger than those that had been obtained using the filter ratio method. Using the energy relation outlined by Rosner et al. (1978), they determined that the heating function was not dominated by radiation or conduction. These results indicated that EUV loops could in fact be multithermal across the loop length as well as through the LOS.

2.3 A controversy is born

In the years to follow, the question of coronal loops shifted from a debate about the thermal properties of the loops to a controversy about the validity of the filter ratio method. In October of 2002, two papers were published in Astrophysical Journal letters suggesting a flaw in the filter ratio method. Martens and Schmelz (2002) and Schmelz (2002) analyzed data from CDS, EIT, and SXT. They added background subtraction to their analysis and used EIT observations to create DEM curves for the same loop that was analyzed in Schmelz et al. (2001.) The DEM curves they obtained were consistent with those that found with CDS data.

Martens and Schmelz (2002) followed up by creating a surface map of the DEM curves. This surface plot was characterized by a broad plateau that shifted towards higher temperatures moving up the length of the loop. This indicates that the plasma was indeed multithermal through the LOS and that higher temperatures are present at the top of the loop. They then conclude that the presence of this plateau could explain the near constant

[4] This process involves manipulating the DEM curve and comparing the intensities it predicts to the intensities with the intensities that were actually observed, with the goal of finding the most statistically probable fit.

isothermal results obtained with the filter ratio method. Schmelz (2002) followed up by simulating the response EIT would have to observing a multithermal loop. Using the filter ratios method, they were able to reproduce isothermal (T = 1.2MK for the 171/195 Å ratio and T = 1.9MK for the 195/284 Å ratio) results for a multithermal loop.

The following month, Aschwanden (2002) attempted to prove that temperature profiles could be recovered using the filter ratio method. He modeled 200 isothermal loops with various sizes and temperatures and concluded that the average temperatures found from the filter ratio method were consistent with the average temperatures found with the DEM method. He then went on to criticize the technique employed by Schmelz et al. (2001) by stating that their DEM curves were "oversmoothed." On this basis, he concluded that filter ratio method is viable.

2.4 The Burden of Proof

Pandora's box had been opened and the question of how to interpret results from filter ratio analysis remained. As is often the case, the person who raises doubt on a matter is left with the burden of proof. Over the next few years, Schmelz and her collaborators set out to prove that the filter ratio technique is unable to conclusively determine the thermal profile of coronal loops.

Following up on concerns about the effect of background subtraction on loop temperature profiles, Schmelz et al. (2003) conducted an analysis of ten loops observed with all three EIT filter. Selecting five pixels for each loop, they used four different background subtraction methods. Using the filter ratio method, they found temperature profiles with the 171/195 Å and the 195/284 Å ratios. The results indicated that the loops

were isothermal[5] and that the background subtraction had very little effect on the temperature profiles. To further their analysis, they applied the same filter ratio method to five pixels that were selected at random. Remarkably, these pixels (that were unrelated to any observed loop structure) produced the same temperature profiles. These results verified that ratio analysis using EIT data did not produce meaningful results for the temperature of the plasma.

In December of 2005, Weber et al. set out to demonstrate the reason why the filter ratio method produced such uniform temperature profiles. They began by showing that the filter ratio method does work for isothermal plasma because there is a one to one relationship between the temperature and the ratio of the response function at that specific temperature[6]. However in a multithermal case, the filter ratio becomes a ratio of integrals[7] given by the equation:

$$\text{Filter Ratio} = I_1/I_2 = [\int P_1(T)dT] / [\int P_2(T)dT], \qquad (4)$$

where P(T) is the response function of filter for a given temperature or temperature range. For the isothermal case, the integral will produce a specific value for a given temperature and thereby a ratio that is specific to that temperature. The multithermal case is best represented by a broad, flat DEM. As the width of the DEM increases, the range of temperatures confining the integrals also increases, exceeding the difference between peak formation temperatures, limits of monotonicity, and eventually encompassing the entirety of one or both of the response functions. This has the effect of allowing many

[5] The temperatures they found were consistent with previous results that produced T = 1.2MK for the 171/195 Å ratio and T = 1.9MK for the 195/284 Å ratio.

[6] A word of caution: This is only true over the range of temperatures where the filter ratio is monotonic (i.e. the range where there is a significant overlap of the response functions), as best illustrated by their Figure 1.

[7] It may be helpful to think of these integrals as areas under a curve.

different temperature profiles to produce the same value for the ratio of integrals (see Figure 5). The temperature parameter essentially becomes lost in the integral and cannot be retrieved. It is important to know that this is not an issue with broadband filters like those used by SXT and XRT. Weber at al. go on to conclude that narrow pass-bands can still be effective in performing temperature analysis, provided that adequate constraints are applied to account for this newly discovered flaw in the filter ratio method. Furthermore, they conclude that this flaw should be taken into consideration when choosing pass-bands to be used for future solar observations.

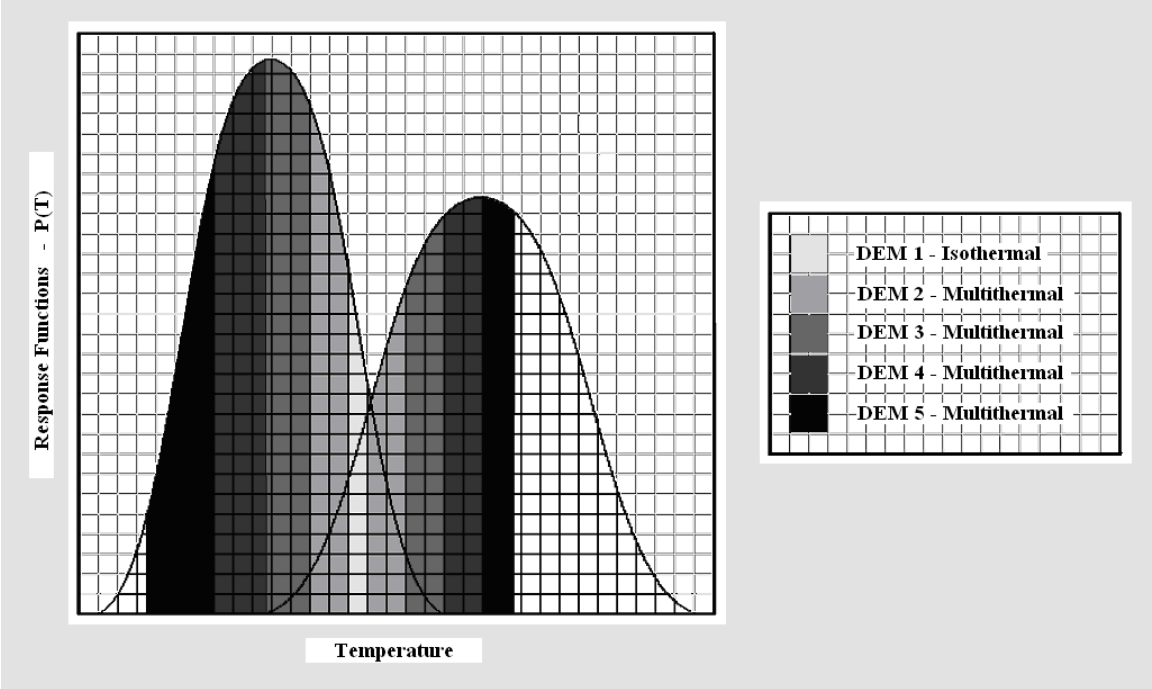

Figure 5*: Response Functions with DEM Overlays. Note that all five DEMs share the same ratios of "area under the curve."*

2.5 Back to the Grind

With the controversy over the filter ratio method resolved, solar physicists returned to the debate that started it all: Are coronal loops multithermal, isothermal, or could there be both? In response to questions about the effect of background subtraction on CDS data, Schmelz et al. (2005) returned to the loop that ignited the filter ratio controversy in Schmelz et al. (2001). They performed a background subtraction[8] on three of the loop pixels. They then compared EM Loci plots obtained with and without background subtraction. They determined that the background was not isothermal. In addition, though the background subtraction had a minor impact on the DEM distribution, the overall loop profile was the same: it appeared multithermal over the loop length and along the LOS. Finally, they compared their results with results from other CDS loops and concluded that not all loops observed with CDS share the same temperature profile. The following year, Schmelz and Martens (January, 2006) revisited the CDS results from Schmelz et al. (2001 and 2005). They applied a background subtraction and used forward folding to determine the temperature profile. Their results were consistent with the prior results that indicated the temperature varied over the loop length.

Aschwanden and Nightingale (2005) searched the TRACE archive for loops present in all three filters in order to isolate and characterize loop strands. They selected 234 loops observed from May 1998 to January 2000 and performed a statistical analysis. They applied a forward fitting method in order to characterize the mean loop width, background, as well as thermal profiles and temperatures. They were able to resolve

[8] Background intensity was determined by averaging the intensity of a pixel inside the loop with the intensity of a pixel outside of the loop).

thinner loops with a mean width of 1400 +/- 300 km[9]. They determined that there was reduced amount of background. They found that both isothermal and multithermal models were viable, but that the majority of the DEMs were isothermal over a large range of temperatures. The following year, Schmelz et al. (2007) examined these results with a probabilistic (MCMC) reconstruction algorithm. Their figure 3 represents the distribution of likely DEMs. They found that there was "no evidence that the TRACE triple-filter data could constrain an isothermal distribution."

2.6 Adding to the Mix

A variety of new analysis methods have been implemented and the race is on to determine conclusively the nature of coronal loops. Results so far indicate that the temperature profile of coronal loops does not fit into one tiny perfectly wrapped package. Rather, the nature of coronal loops appears to be more diverse. One thing that has been clearly demonstrated is that before a heating model can be established, more loops need to be analyzed. As instruments and analysis techniques continue to improve, the next generation of solar physicists can build on the foundation that has painstakingly laid and hopefully come closer to solving the mystery of coronal heating. The purpose of this work is to do just that: use data obtained from latest, most advanced instruments to provide additional analysis of coronal loops to the solar physic community. Chapter 4 will discuss the details of the analysis and the results of two loops observed by the EIS and XRT instruments.

[9] Although, they could not determine if smaller widths were present.

3. Instruments

The data analyzed for this project came primarily from two instruments, the Extreme Ultraviolet Imaging Spectrometer (EIS) and the X-Ray Telescope (XRT), aboard the satellite HINODE. Launched September 22nd of 2006 at 21:36 GMT, HINODE is the newest satellite to study the Sun and provides the highest resolution images of the Sun in the optical, EUV, and X-Ray wavelengths. This chapter will begin with a section discussing the HINODE mission and spacecraft. The next two sections will discuss the EIS and XRT instruments in greater detail. The chapter will conclude with a section outlining the process for obtaining EIS and XRT data for analysis.

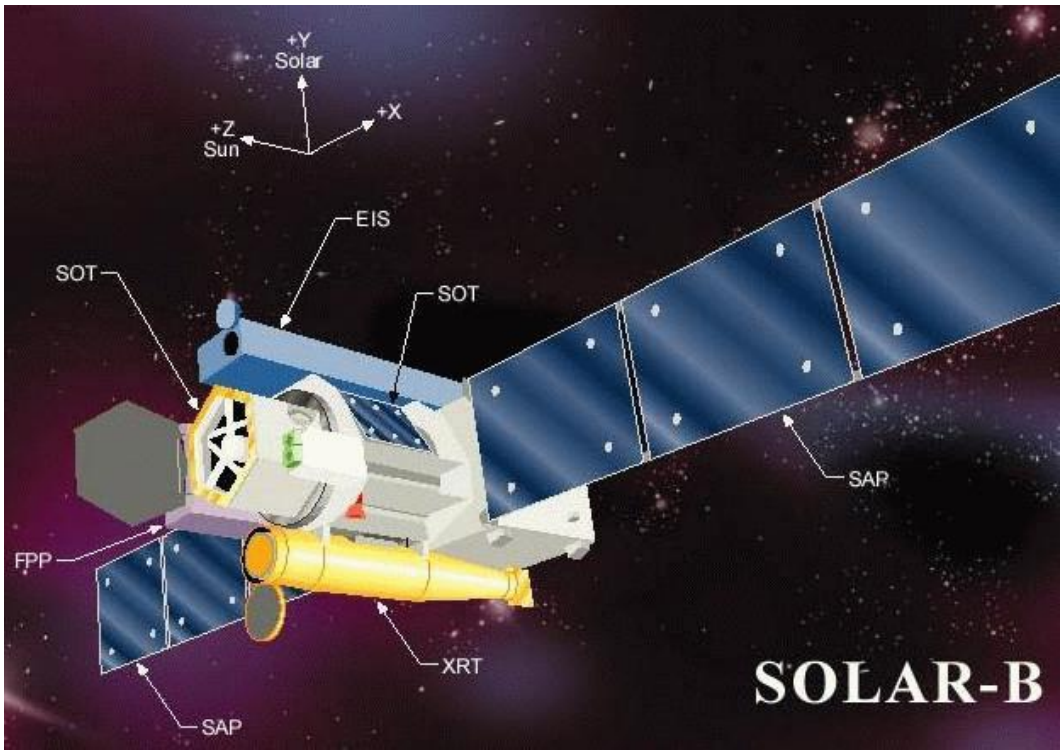

Figure 6: *HINODE. (Courtesy of NASA.) This image shows an artists rendering of HINODE, known as Solar-B prior to launch, and its instruments.*

3.1 HINODE

Originally know as Solar-B, because of the Japanese custom of only naming a satellite after a successful launch, HINODE is Japanese for Sunrise. The HINODE mission is led by the Institute of Space and Astronautical Science of the Japan Aerospace Exploration Agency (ISAS/JAXA). HINODE's conception was largely brought about by the huge success of ISAS's previous Yohkoh mission[1]. Launched in 1991 and lasting for just over a decade, Yohkoh showed the world how vital observations in the X-ray wavelengths are to the study of the Sun. With the demise of Yohkoh, HINODE soon filled the role of our window to the extremely dynamic and structured, yet still not completely understood, high energy solar corona.

While HINODE was launched and is led by ISAS/JAXA, several organizations across the world have come together to make it all possible. The spacecraft was designed and built by the National Observatory of Japan (NAOJ). NAOJ, NASA and the Science and Technology Facilities Council (STFC) are responsible for the instruments aboard HINODE. Ground stations are maintained and operated by Uchinoura Space Center, JAXA, the European Space Agency (ESA), and The Norwegian Space Centre.

The primary goal of HINODE is to study the complex, and typically convoluted, solar magnetic fields. More specifically, HINODE will investigate:

- Magnetic fields (creation, transport, reconnection)
- Variations in solar luminosity (as related to magnetic fields)
- Solar eruptions (i.e. flares, coronal mass ejections)
- Coronal heating mechanisms

[1] Further information about the Yohkoh mission can be found at http://www.lmsal.com/SXT/main.html.

To accomplish these goals, HINODE houses three observing instruments: Solar Optical Telescope (SOT), the Extreme Ultraviolet Imaging Spectrometer (EIS) and the X-Ray Telescope (XRT). Working in conjunction, these three instruments provide simultaneous data about magnetic phenomena in optical, EUV, and X-Ray wavelengths. Furthermore, HINODE's Sun-synchronous orbit[2] allows these instruments to observe the Sun constantly for nine months at a time.

Uchinoura Space Center and JAXA send observation commands to HINODE. The Mission Data Processor (MDP) processes the commands and creates observation tables which run the SOT and XRT. EIS processes the commands and creates its own observation table. HINODE also features the unique ability to monitor for solar flares. In the event of a solar flare, a signal is sent to the observation tables to halt the commands from ground control and the instruments enter a special mode for observation of the flare. Observational data obtained by all three instruments are sent to the MDP to be compressed before being sent to the Data Recorder, which can store up to 8 Gbits. The data is then downloaded by the Uchinoura ground station 4 times per day and the Norwegian (Svalbard) ground station 15 times per day. Finally, the data is sent to the ISAS to be converted to FITS files and stored in the ISAS Sirius database. The data is also mirrored and kept at other locations such as the Solar Data Analysis Center (SDAC) and the Mullard Space Science Laboratory (MSSL).

[2] This orbit is obtained by maintaining a circular polar orbit with an inclination of 98.1° at an altitude of 680km and a period of 98 minutes.

3.2 EIS

EIS was designed, built and tested by the MSSL, ISAS/JAXA, NAOJ, the US Naval Research Laboratory (NRL), Rutherford Appleton Laboratory (RAL), Birmingham University, and the University of Oslo. EIS is a spectrometer with two CCDs designed for viewing light in the EUV wavelengths, 170 - 210 Å and 250 - 290 Å. At these wavelengths, EIS is ideal for imaging the top of the transition region and the solar corona. Light enters EIS through an Al filter, limiting the amount of light from optical wavelengths. The light is then reflected from the primary mirror through a slit (with an aperture of 1,2,40, or 266 arc secs), through a second Al filter and onto a grating. The light then passes onto the two CCDs as shown in Figure 7.

EIS specifications include a temperature range of $6.0 < \log T < 7.3$, a spatial resolution of 2 arcsecs, and a field of view (FOV) of 6 arcmins by 8.5 arcmins. Its spectral and spatial resolutions are able to produce unparalleled images[3] of active regions for several strong emission lines simultaneously. A comparative analysis of the emission

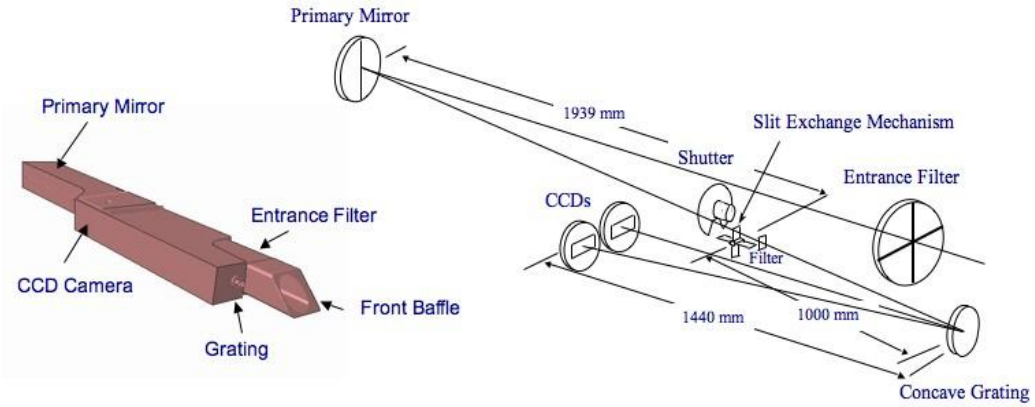

Figure 7: *EIS Optical Diagram. (Courtesy of NASA.) This image shows the layout inside the EIS instrument.*

[3] This resolution provides a significant improvement over its predecessor, the Coronal Diagnostic Spectrometer.

line intensity as a function of wavelength can then be used to determine the thermal and density properties of the plasma.

3.3 XRT

XRT was designed, built and tested by the Smithsonian Astrophysical Observatory (SAO), ISAS/JAXA, NAOJ, and NASA. XRT is a telescope designed for viewing light in the x-ray wavelengths, specifically 2 - 200 Å. The most significant constraints to its design were a temperature range of $6.1 < \log T < 7.5$ and a temperature resolution of $\log T = 0.2$. Additional requirements included an exposure time of 4 ms - 10 s (with 2 s between exposures), a spatial resolution of 2 arcsecs, and a field of view (FOV) of more than 30 arcmins. These specifications make XRT ideal for imaging features such as solar flares and jets, coronal mass ejections, coronal loops, and coronal holes. Furthermore, these specifications make it a great tool for studying the mechanisms behind coronal heating and magnetic reconnection as well as the relationship between the photosphere and the corona and how energy is transferred between the two.

Light that enters XRT (see Figure 8) begins by passing through a filter designed to limit the amount of light from optical wavelengths that enter the telescope. The telescope features a grazing incidence mirror[4] that focuses light onto a CCD at the end of the telescope. Two additional filter wheels (see Table 4) have been placed between the mirror and the CCD, further limiting the wavelengths that can pass through to the CCD. Thicker filters only allow higher temperature wavelengths to pass through and thus are better for viewing high energy events such as solar flares.

[4] A special optic has also been included to allow for the collection of data in the optical (G-band) wavelengths.

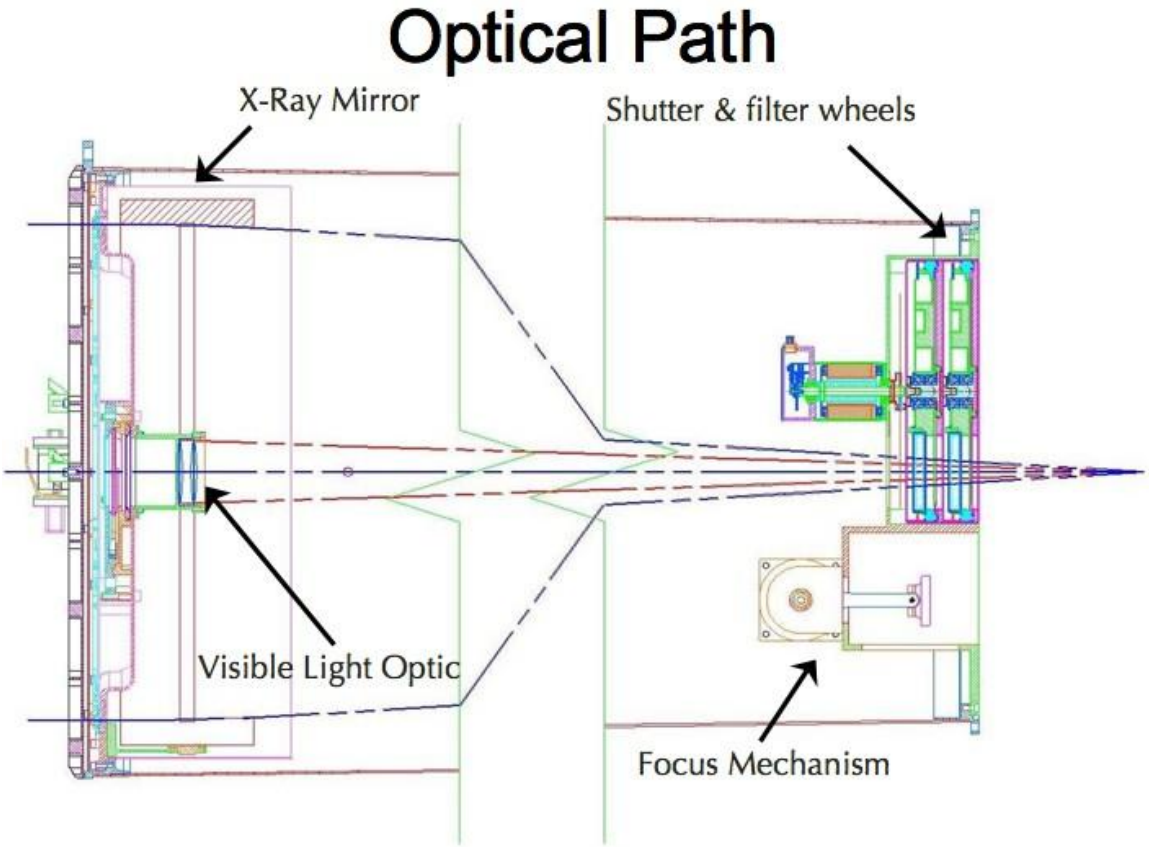

Figure 8: *XRT Optical Path. (Courtesy of Golub et al, 2007.) This image shows the optical path of light that enters the XRT instrument.*

Table 4: *Filter Wheels and Filter Thicknesses*

Filter 1	Thickness (Å)	Filter 2	Thickness (Å)
Thin Al-Poly	1250	G-band	
C-Poly	6000	Thin Al-Mesh	1600
Thin Be	90000	Ti-Poly	3000
Med Be	300000	Thick Al	250000
Med Al	125000	Thick Be	3000000

3.4 Obtaining Data

EIS and XRT data were used for the coronal loop analysis described in Chapter 4. These data are made available online to the general scientific community. This section will outline the procedure for obtaining data observed by each of these instruments.

EIS data is available through a search engine at the following URL:

http://msslxr.mssl.ucl.ac.uk:8080/SolarB/SearchArchive.jsp

The search form begins by asking for a Start Date/Time and End Date/Time[5]. Clicking "Submit entry" will produce a list of the available data sets. The name of the FITS file, the type of target (active region, or quiet Sun), the slit size, and the observation type will also be shown. At the end of the entry will be a button (labeled with the entry number) that can be pushed to produce thumbnails of the EIS FOV and the intensity maps. Clicking on one of these thumbnails will bring up a larger version of the image[6]. Going back to the FITS list page, "Select" box should be checked for each data set to be analyzed. Once all data has been selected, the users e-mail address should be entered and the "Request Files" button should be selected. The data will then be processed and then a link to data (all compressed into a single .zip file) will be sent to the e-mail address.

XRT data can be obtained by using the SAO Hinode / XRT Search Form at the following URL:

http://kurasuta.cfa.harvard.edu/cgi-bin/VSO/prod/searchForm.pl?time=1&instrument=1&version=current&build=1&provider=SAO&prov_excl=1

The search form will prompt the user to enter a Start Date/Time and End Date/Time. The

[5] Advanced users may also SQL to create customized searches.

[6] This is useful for identifying which emission lines have a significant contribution to a loop.

user may also click on “Show Advanced Options” to include the search criteria shown in Table 5. Clicking “Search” will pull up observation entries that match the selected criteria. Entries will be listed according to observation time. Additional information about the Filters, FOV, exposure time, etc. will also be displayed. Clicking on “Thumbnail” at the beginning on an entry will produce a preview of what the image looks like. The check box at the beginning of each entry will allow the user to mark entries for analysis. Once all data has been marked, the “Request Data” button on the bottom left side of the screen will select the marked data. Checking “URL-File” and clicking on the “Request Data” button below that will produce a page with links to FITS files of the marked entries. These files will need to be downloaded individually[7].

Table 5: *XRT Advanced Search Options*

Category	Options
Extent	Full Sun
Darks	Ignore Darks, Include Darks, Darks Only
Filter 1	None, Thin-Al/Poly, C/Poly, Thin-Be, Med-Be, Med-Al
Filter 2	None, Thin-Al/Mesh, Ti/Poly, G-Band, Thick-Al, Thick-Be
FOV	=, >=, <=, Any
	2048 x 2048, 1024 x 1024, 512 x 512, 256 x 256
Exposure	=, >=, <=
	____ Seconds
Binning	Any, 1, 2, 4, 8
Location	NE, SE, SW, NW

[7] It is best if FITS files are grouped in separate folders by image size.

4. Methods and Analysis

The purpose of this thesis is to analyze coronal loop data observed by the EIS and XRT instruments aboard HINODE and to determine the thermal and density properties of those coronal loops. The region of interest was selected based on the presence of hot X-ray loops observed by both instruments as well as the presence of Fe XV and Fe XVI emissions. The loops in this analysis were located in Active Region (AR) 10978, which was monitored by HINODE in December 2007. EIS began its observation of these loops at 00:12:26UT on 12/09 using a 1" slit. It took approximately one hour to process the entire EIS field of view, shown in Figure 9. XRT data from the same region were also used. XRT observations were made with the Ti Poly filter (12/09 00:02:31UT), the Be Thin filter (12/09 00:08:06UT), and the Thin-Al Poly / Ti Poly filters (spanning 12/08 22:31:36UT to 12/09 00:56:33UT).

Analysis of the data was done with the Interactive Data Language (IDL), the preferred programming language of solar space physicists. The Solar Soft package, maintained by Lockheed-Martin, was used to prepare the data. Specialized routines for each instrument were created by the EIS and XRT teams respectively[1]. EIS_prep.pro and XRT_prep.pro were used to calibrate the data. The data were also de-spiked and checked for saturation. The EIS instrument is a spectrometer; therefore data obtained with EIS must be split into its spectral components in a process known as spectral line fitting. This was done with the EIS_auto_fit routine. The XRT data has contamination from spots that appeared on the CCD. The XRT_cat and XRT_tup_contam routines were used to mark these spots so that they would not be used in the analysis. Both the EIS and XRT data

[1] EIS data preparation guide: http://solar.bnsc.rl.ac.uk/~young/solarb_eis/paris_tutorial/ and XRT data preparation guide: http://xrt.cfa.harvard.edu/science/XRT_tutorial_data2.txt.

were manually co-aligned to account for instrumentation offsets. Atomic physics data was obtained using CHIANTI version 5.2 (Dere et al. 1997). The Fludra and Schmelz (1999) coronal elemental abundances and the Mazzotta et al. (1998) ionization balances were also used in the analysis.

The EIS data for the loops in this analysis contain several strong Fe lines. Table 6 contains a list of these ions, the wavelengths in Angstroms, and the log of their peak formation temperatures. Figure 10 shows the individual images for each EIS spectral line used. In addition, these data also include multiple density sensitive Fe pairs: FeXII 186.88Å to 193.51Å and 186.88Å to 193.51Å, Fe XIII 203.83Å to 202.04Å, and Fe XIV 264.78Å to 274.2Å.

Two loops were selected for analysis and are marked on the Fe XV 284.16 EIS image in Figure 11. Loop 1 is the nearly vertical loop on the right side of the region. Loop 2 is the curved loop on the left side of the region. Prior to analysis, loop emission intensity was isolated by removing background (BG) emission from each pixel. Emission intensity is measured in ergs/cm^2/s/ster. The BG intensities were determined by taking cuts across the loop and then creating linear fits to these cuts. Cuts were made at y = 113, y = 123, and y= 133 for Loop 1 (see the dashed lines in Figure 11). Cut were made at y=132 through y = 137 for Loop 2 (the box in Figure 11).BG intensities were then subtracted from each loop pixel to obtain BG subtracted intensities which represent the isolated loop intensity. Figure 12 demonstrates this technique using a cut across the Loop 1 at y = 113 for the Fe XV 284.16 spectral line.

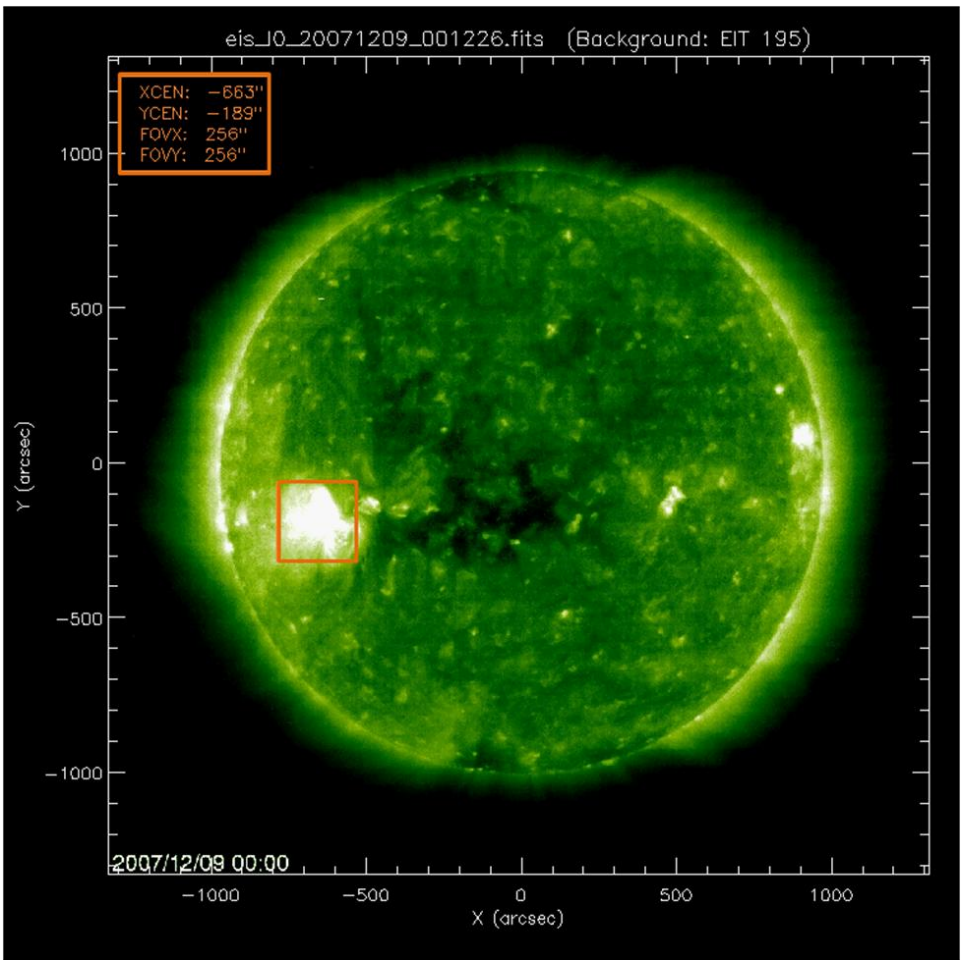

Figure 9: *EIS Field of View. (Courtesy of http://msslxr.mssl.ucl.ac.uk:8080/SolarB/Solar-B.jsp.) This image shows the EIS field of view for Active Region 10978 overlaid onto a full image of the Sun as seen by EIT 195Å.*

Table 6: *EIS Spectral Line List*

Ion	λ(Å)	log (T)
Fe X	184.54	6
Fe XI	188.23	6.1
Fe XII	186.88	6.1
Fe XII	193.51	6.1
Fe XII	195.12	6.1
Fe XIII	202.04	6.2
Fe XIII	203.83	6.2
Fe XIV	264.78	6.3
Fe XIV	274.2	6.3
Fe XV	284.16	6.3
Fe XVI	262.98	6.4

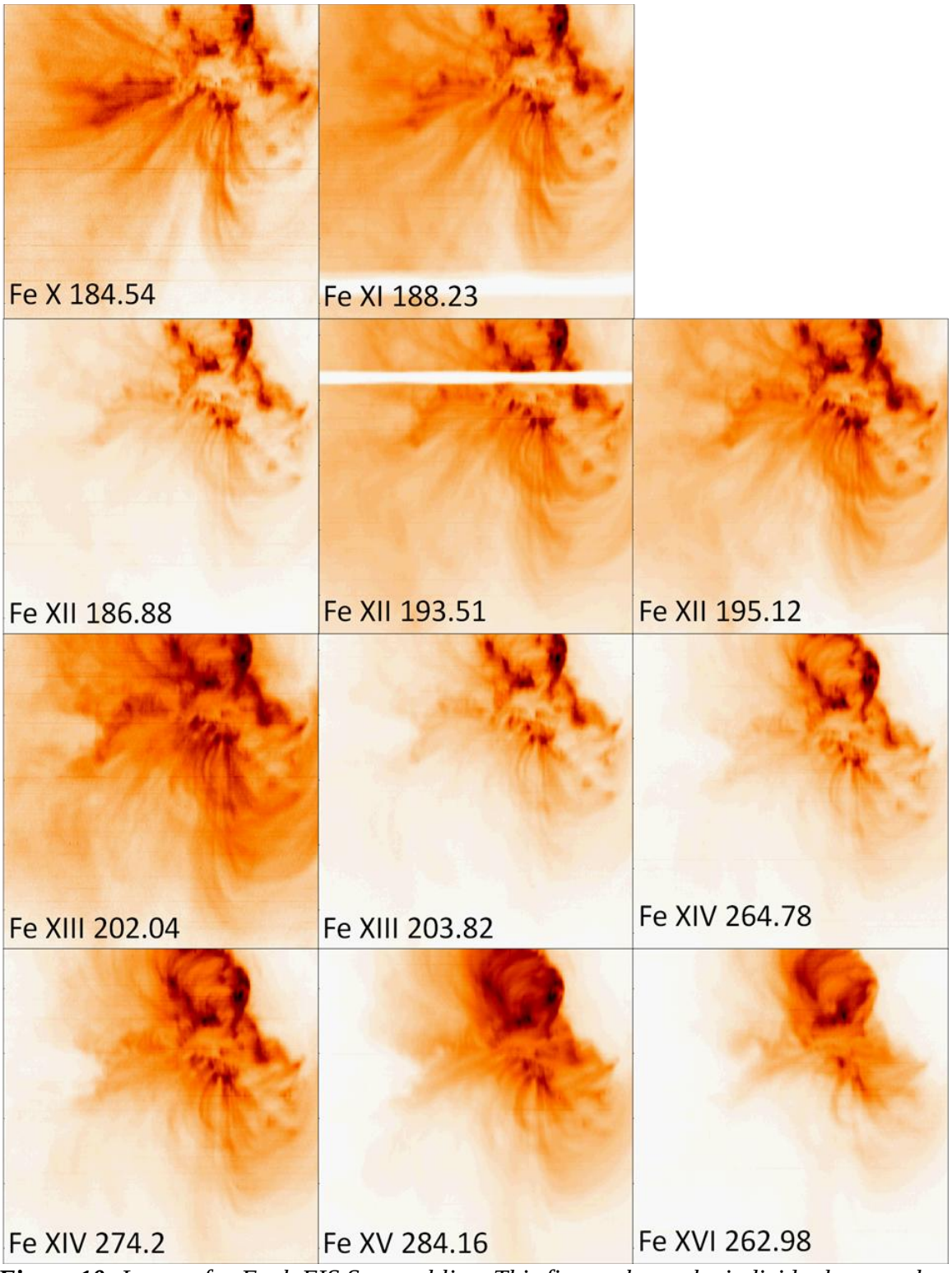

Figure 10: *Images for Each EIS Spectral line. This figure shows the individual spectral images for each of the EIS lines used in this analysis.*

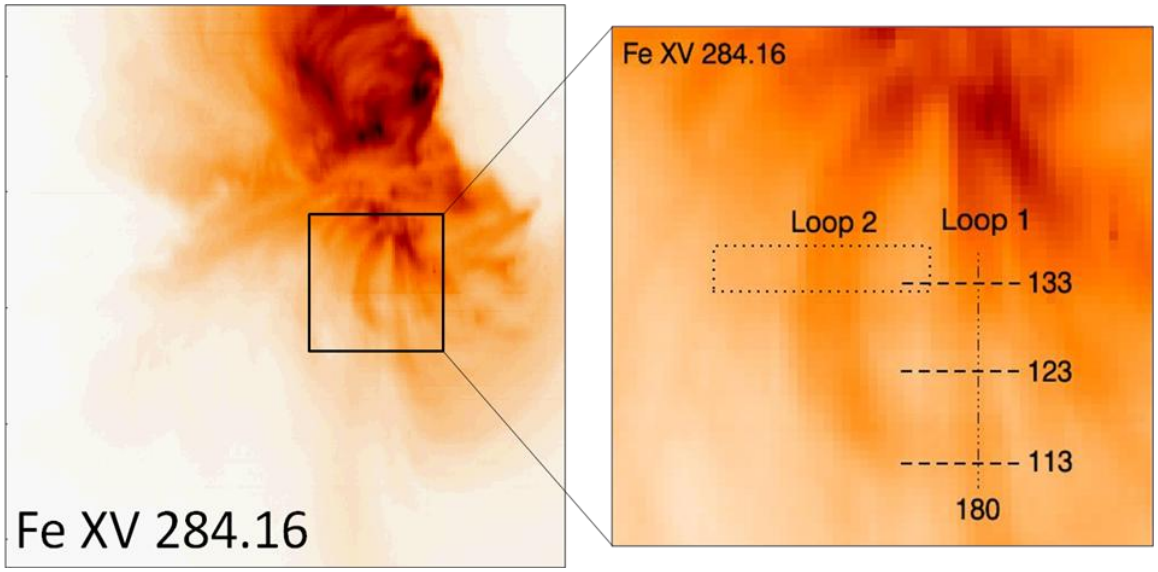

Figure 11: *Analyzed Loops. This figure zooms into the EIS Fe XV spectral line image to show loops that were analyzed. Loop 1 is the nearly vertical loop on the right and loop 2 is the curved loop on the left.*

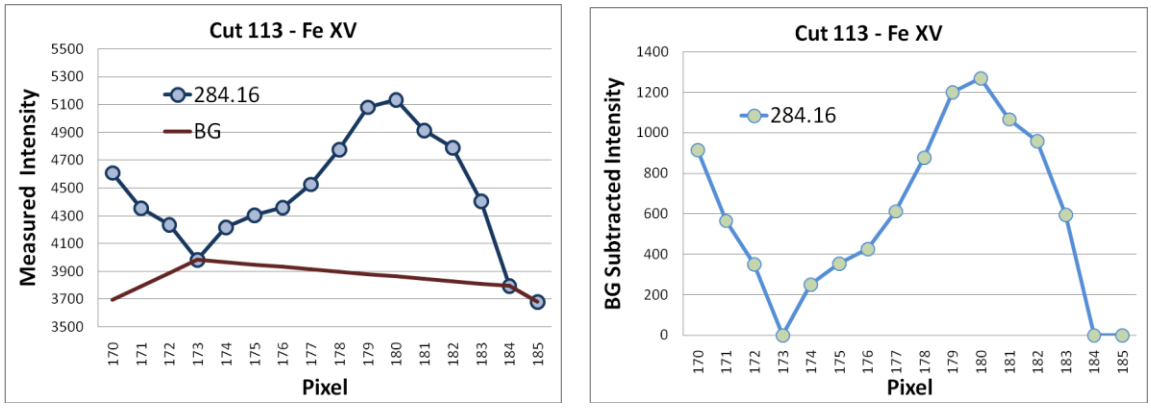

Figure 12: *Background Subtraction Method.A cut is taken across the loop and the measured intensities are plotted. The BG intensity is determined by creating a linear fit to the measured intensity cut. This is then subtracted to obtain the BG subtracted intensity, or isolated loop intensity.*

4.1 Loop 1

After BG subtraction, this loop had a peak intensity along the vertical line corresponding to x = 180 for all three cuts. Three pixels along the loop were selected for analysis: pixels (180, 113), (180, 123), and (180, 133). As shown in Figure 11, all three pixels are located on the leg of the loop with pixel (180, 133) being closest to the footpoint of the loop. These pixels will henceforth be referred to as pixels 113, 123, and 133. Finally, BG subtraction also revealed that pixel 113 did not have significant emission from the Fe X 184.54 and Fe XI 188.23 spectral lines[2], therefore the contributions from these lines were not considered in the analysis of pixel 113.

The initial density analysis of this loop was done by examining the density sensitive iron pairs. Depending on the atomic physics, the percentage of transitions for certain ionizations will change as a function of electron density. This allows the predicted ratio of intensities for two different spectral lines, given by the CHIANTI atomic physics database, to be plotted as a function of density. By comparing the measured ratio of intensities to this plot, a density (in cm^{-3}) is obtained, as demonstrated with data from pixel 123 in Figure 13. Electron densities for each of the three pixels, listed in Table 7, were obtained for two Fe XII pairs, a Fe XIII pair, and a Fe XIV pair. These densities were then averaged to obtain densities to use as the starting densities for the thermal analysis[3]

The first type of thermal analysis is a technique known as Emission Measure (EM) Loci, where EM is simply the amount of emitting material and Loci refers to the

[2] This was also confirmed by visual inspection of the individual EIS images.

[3] These densities will later be refined during the thermal analysis process.

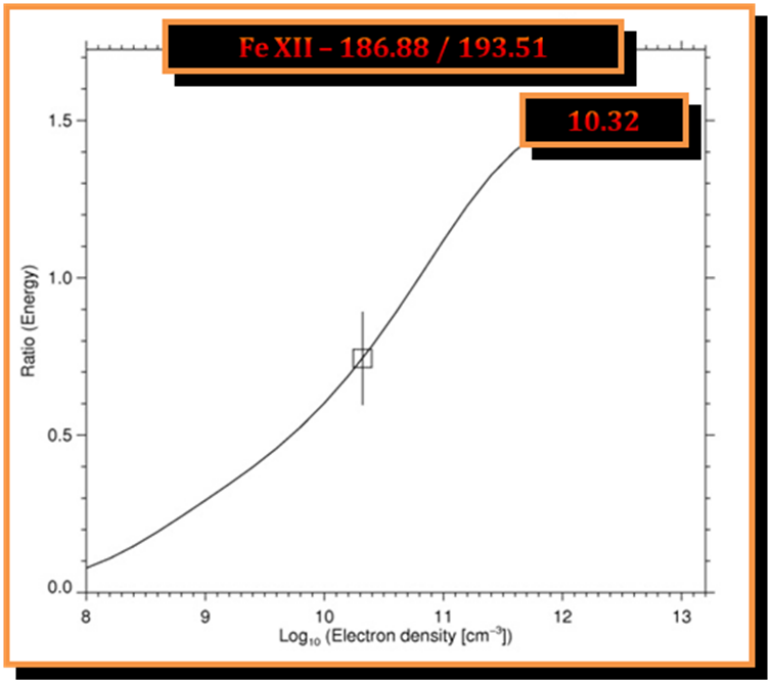

Figure 13: *Density Analysis Method. The predicted ratio of the Fe XII pair, 186.88Å to 193.51Å obtained from CHIANT is plotted. The ratio of measured intensities for pixel 123 is then plotted over this, the intersection of the two produces a log (density) of 10.32.*

Table 7: *Densities for Loop 1 Pixels.*

Pixel	Ion	λ	λ	Ratio	Density	log(Density)
Pixel 113	Fe XII	186.88	195.12	0.4484	1.5E+10	10.16
	Fe XII	186.88	193.51	0.6239	1.2E+10	10.06
	Fe XIII	203.83	202.04	2.6590	1.1E+10	10.04
	Fe XIV	264.78	274.2	0.7391	5.8E+08	8.76
Pixel 123	Fe XII	186.88	195.12	0.4739	1.7E+10	10.24
	Fe XII	186.88	193.51	0.7440	2.1E+10	10.32
	Fe XIII	203.83	202.04	2.8572	1.6E+10	10.2
	Fe XIV	264.78	274.2	0.7644	6.9E+08	8.84
Pixel 133	Fe XII	186.88	195.12	0.3998	9.6E+09	9.98
	Fe XII	186.88	193.51	0.6016	1.0E+10	10
	Fe XIII	203.83	202.04	2.9805	2.1E+10	10.32
	Fe XIV	264.78	274.2	0.9590	1.7E+09	9.24

convergence to a point. EM Loci assumes an isothermal approximation, i.e. that the loop plasma is at a single temperature. Given the intensity for a spectral line, this approximation allows the EM to be plotted as a function of temperature. With an isothermal result, the EMs for all the spectral lines are expected to all intersect near a single loci. The temperature at that intersection would be the temperature of the loop plasma. However, if the EMs fail to converge, the result is considered to be inconsistent with an isothermal plasma. Figure 14 shows the EM loci plots for pixels 113, 123, and 133. In all three cases the EMs intersect over a broad range of temperatures. While this does not lead to a specific temperature, these results may still be used to constrain DEM results that indicate a multi-thermal plasma.

The second type of thermal analysis, Differential Emission Measure (DEM) analysis, allows the user to investigate both isothermal and multi-thermal models. Two different DEM techniques were used in this analysis: DEM Interactive and DEM Manual. Both techniques are used to find DEM profiles that produce predicted intensities for each spectral line. These predicted intensities are then compared to the observed intensities and a χ^2 is calculated. Best DEM models are found by minimizing the χ^2. While the DEM Interactive process is automated and quick, the DEM Manual allows more input from the user. With the DEM Interactive technique, the user creates a very basic DEM shape using a set of spline knots. The software then makes a series of calculations designed to find the DEM that produces the best χ^2. The user can experiment with variations in the initial positioning of spline knots, typically producing similar results. This technique is limited by the smoothing inherent in the calculations, causing the DEMs to appear broader and more curved.

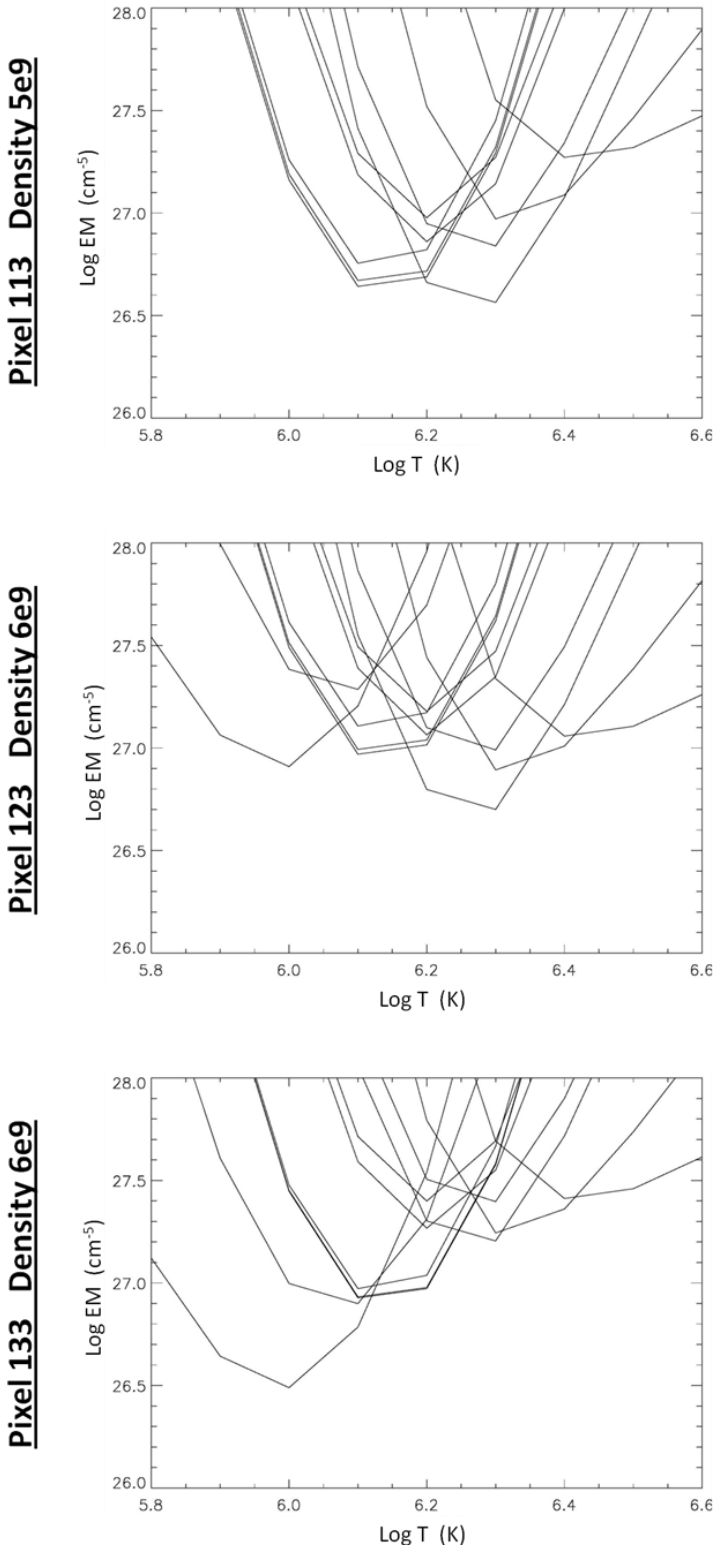

Figure 14: *EM Loci Analysis. For all three pixels, the lines intersect over a range of temperatures. This is not consistent with and isothermal result.*

The DEM Manual technique allows the user to manually create a DEM profile to test. The user then adjusts the DEM with the aid of a set of predicted-to-observed intensity ratios for each spectral line in the dataset as well as the χ^2. The user can then make subtle or dramatic changes to the DEM while attempting to find a solution that produces the best fit. This allows the user to test a variety of different DEM profiles: narrow and spiky, broad and flat, or even DEMs with more than one component. However, this requires the user to have a firm understanding of what assumptions can be made from the data and their impact on the DEM, how changes in the DEM affect the goodness of fit, and how to interpret the results.

Once a DEM is found, addition density analysis can also be performed by varying the density. By observing how these variations affect the χ^2 and the agreement of density sensitive line pairs, the user is able to find a weighted density that best fits the data. Due to the limitless number of DEMs and subtle modification that can be made, this process is quite time consuming, especially if the user tests multiple DEM models. The additional density analysis offered by DEM Manual produced weighted densities of 6e9 for pixels 123 and 133 and a density of 5e9 for pixel 113.

The results of the thermal analysis for Pixel 113 are shown in Figure 15. The DEM Interactive technique (top plot) found a broad DEM, with a Log T distribution between 5.9 and 7.1. The DEM Manual results also show a broad DEM (middle plot) with a Log T between 6.1 and 6.6[4]. The ratio scatter plot from the DEM Manual analysis (bottom plot) shows a χ^2 of 1.3.

[4] Recall that the DEM Iterative is subject to additional smoothing, therefore it is not surprising that it produces a larger range of temperatures than found in the DEM Manual analysis.

Figure 16 shows the thermal analysis for Pixel 123. The DEM Interactive plot (top) shows a broad DEM, with a Log T distribution between 5.3 and 6.9. The DEM Manual also produces a broad DEM (middle) with a Log T between 5.8 and 6.6. A χ^2 of 3.2 is shown in the ratio scatter plot from the DEM Manual technique (bottom).

The thermal analysis for Pixel 133 is show in Figures 17. The DEM Interactive results (top) show a broad DEM, and a Log T distribution between 5.7 and 6.5. The DEM Manual results also show a broad DEM (middle) with a Log T between 5.8 and 6.6. The DEM Manual ratio scatter plot (bottom) gave a χ^2 of 4.8.

It is important to note the difference seen between the DEM profiles obtained by DEM Interactive and DEM Manual. While DEM Manual produced relatively simple shapes, the profiles found by DEM Interactive are characterized by unusual dips. While one might be tempted to attribute these dips to some physical significance, but care should be taken not to do so. As mentioned before, the DEMs obtained with DEM Interactive are quickly found using a calculation designed to minimize the χ^2. These calculations are based not only on the observations, but also on the atomic data. Unfortunately, atom physics is an evolving science and a great deal of uncertainty still exists in the atomic data. This gives rise to the potential for DEM Iterative to produce shapes that are dominated by these uncertainties in order to obtain the best χ^2. While profiles obtained with DEM Iterative provide a quick approximation to the DEM, arbitrary significance should not be inferred without additional support from the data. This further demonstrates the importance of the flexibility offered by DEM Manual.

Examination of the ratio scatter plots reveal that the predicted to observed ratios for Fe XI were significantly small (ratio ~ 0.5) for both pixels 123 and 133. In both cases,

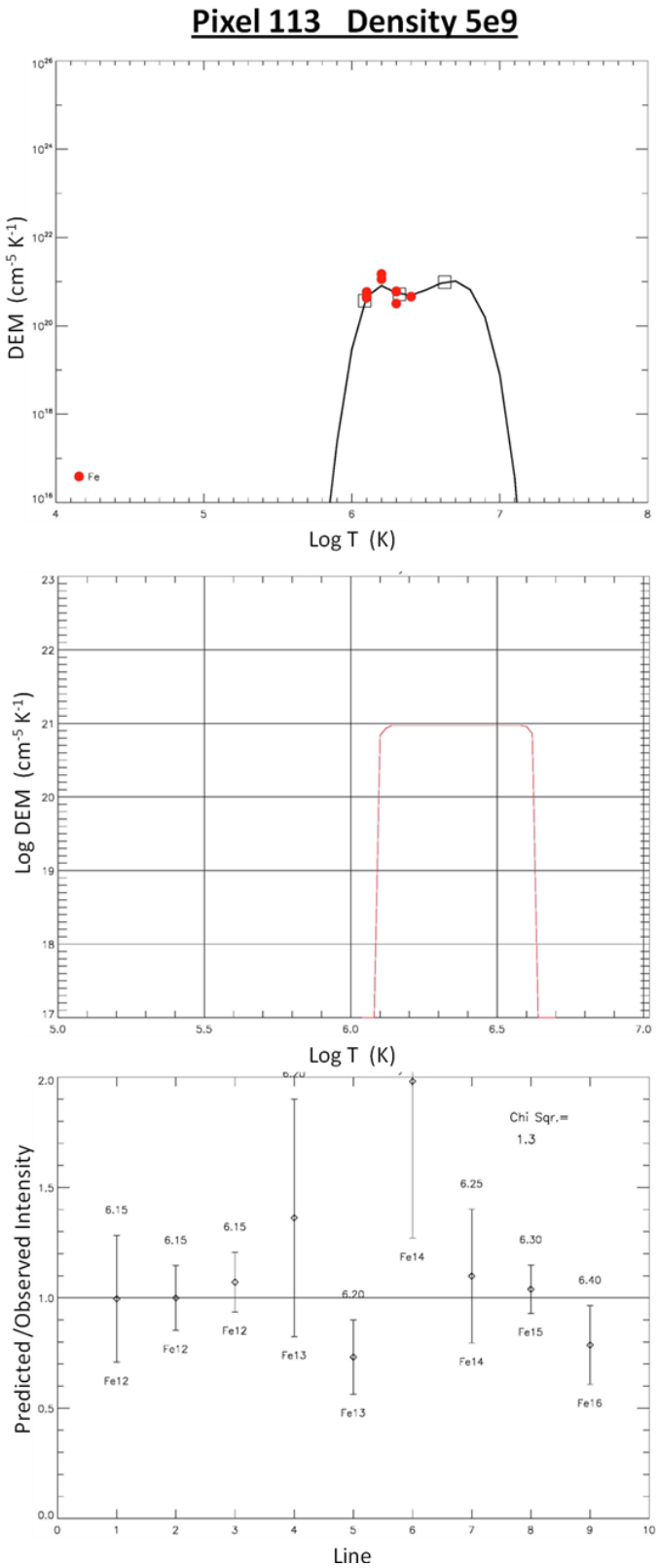

Figure 15: *DEM Analysis of Pixel 113. The DEM Interactive plot (top) shows a broad DEM. The DEM Manual plots (middle and bottom) also show a broad DEM and a Chi Square of 1.3.*

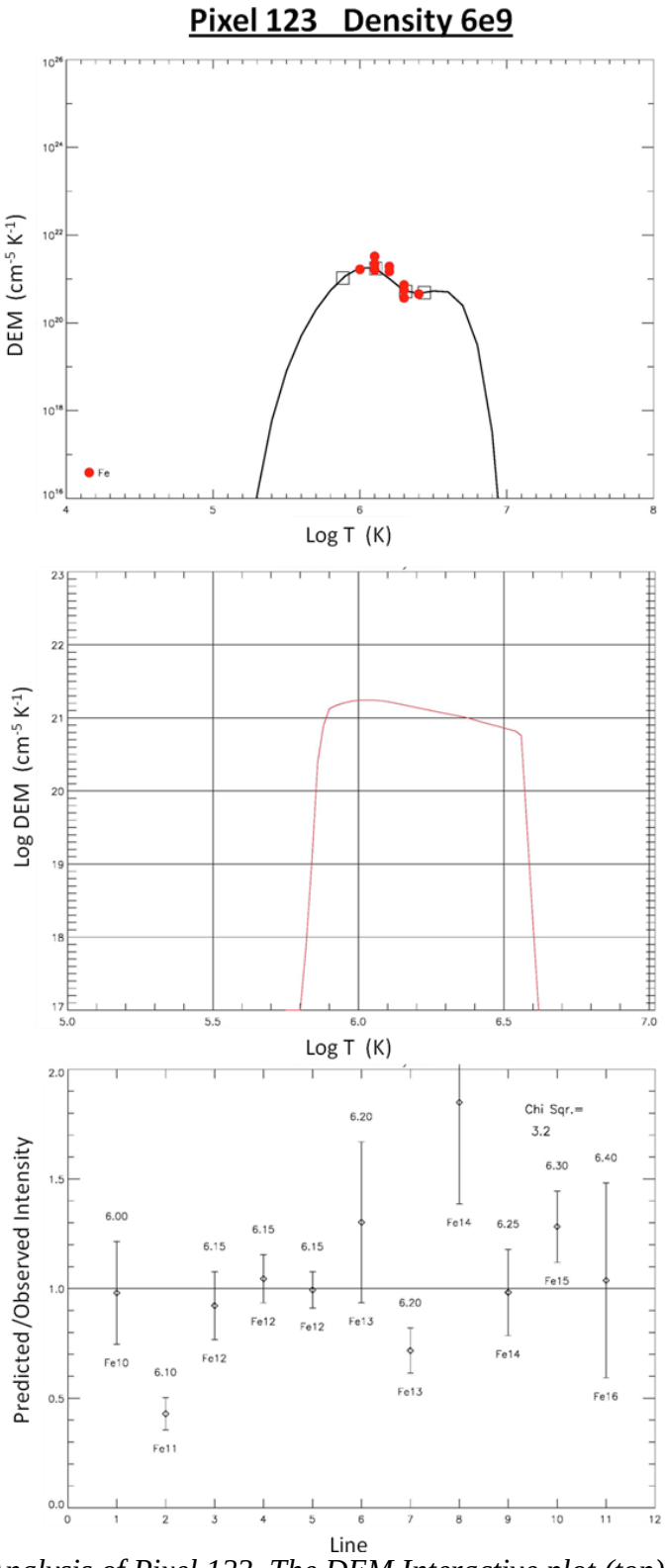

Figure 16: *DEM Analysis of Pixel 123. The DEM Interactive plot (top) shows a broad DEM. The DEM Manual plots (middle and bottom) also show a broad DEM and a Chi Square of 3.2.*

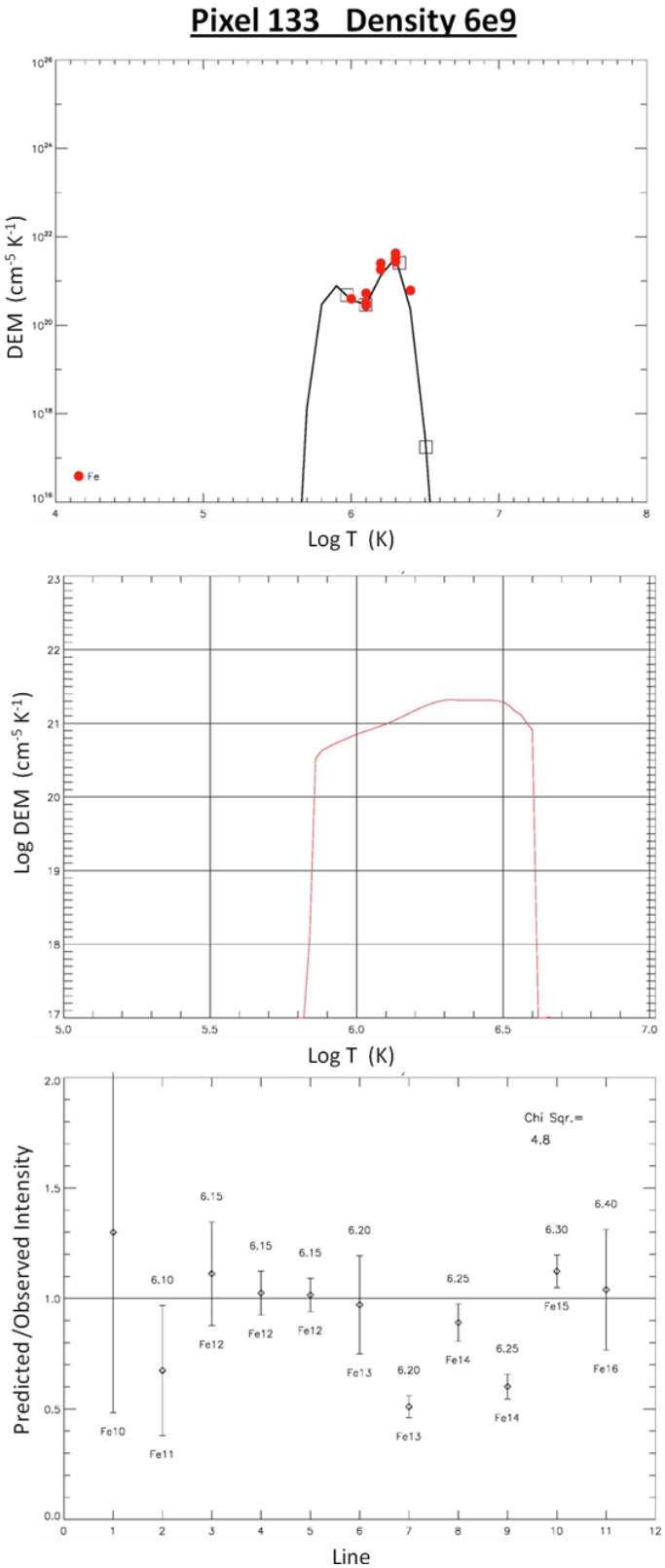

Figure 17: *DEM Analysis of Pixel 133. The DEM Interactive plot (top) shows a broad DEM. The DEM Manual plots (middle and bottom) also show a broad DEM and a Chi Square of 4.8.*

the Fe XI is constrained by the Fe X line and the Fe XII lines. While the χ^2 values obtained in this analysis were quite good, they would have been significantly improved if the Fe XI had had a better fit. Shmelz et al. (2009) also found Fe XI ratios did not fit well with the rest of the EIS data. This is additional support that the atomic physics of the Fe XI needs to be reviewed.

The DEMs for all three loops span a large range of temperatures, suggesting the loop in multi-thermal along the line of sight (LOS). While the temperature profiles of all three pixels extends to Log T = 6.6, there appears to be some loss of the low temperature plasma (Log T ~ 5.8-6.1) in pixel 113, the farthest from the footpoint. These results are consistent with the appearance of the loops in the individual EIS spectral imaged, which show a that the Fe X and XI begin to fade out between pixel 113 and 123. The analysis of Loop 1, indicating multi-thermal plasma with a temperature that varies over the loop length, are similar to the CDS results of Schmelz et al. (2001 and 2005) and Schmelz and Martens (2006).

Recall from chapter 2, the standard model (Rosner et al. 1978) requires that T_{Max} of the loop must occur at the top of the loop in order to maintain equilibrium between a steady heating mechanism and the radiative and conductive losses. The absence of the cooler emission moving away from the footpoint, as seen in pixel 113, is consistent with the standard model. However, a significant increase in emission is seen near Log T = 6.3 in pixel 133, the closest to the footpoint. The increase in temperature near the footpoint means that this loop cannot be characterized by the standard model alone; i.e. an unstable heating mechanism may be at work.

4.2 Loop 2

Loop 2 is at more of an angle than Loop 1 and therefore appears to have a more curved shape. In order to reduce the amount of noise in the data, cuts across the loop were selected at y = 132-137[5] and were averaged for each spectral line. BG subtraction was then carried out as described at the beginning of this chapter. Unfortunately, after BG subtraction, the loop did not appear to peak at any one x value. Figure 18 shows higher temperature emissions peak near pixel 163, however the peaks in intensity appear to spread out symmetrically from pixel 163 as the formation temperature of the emission

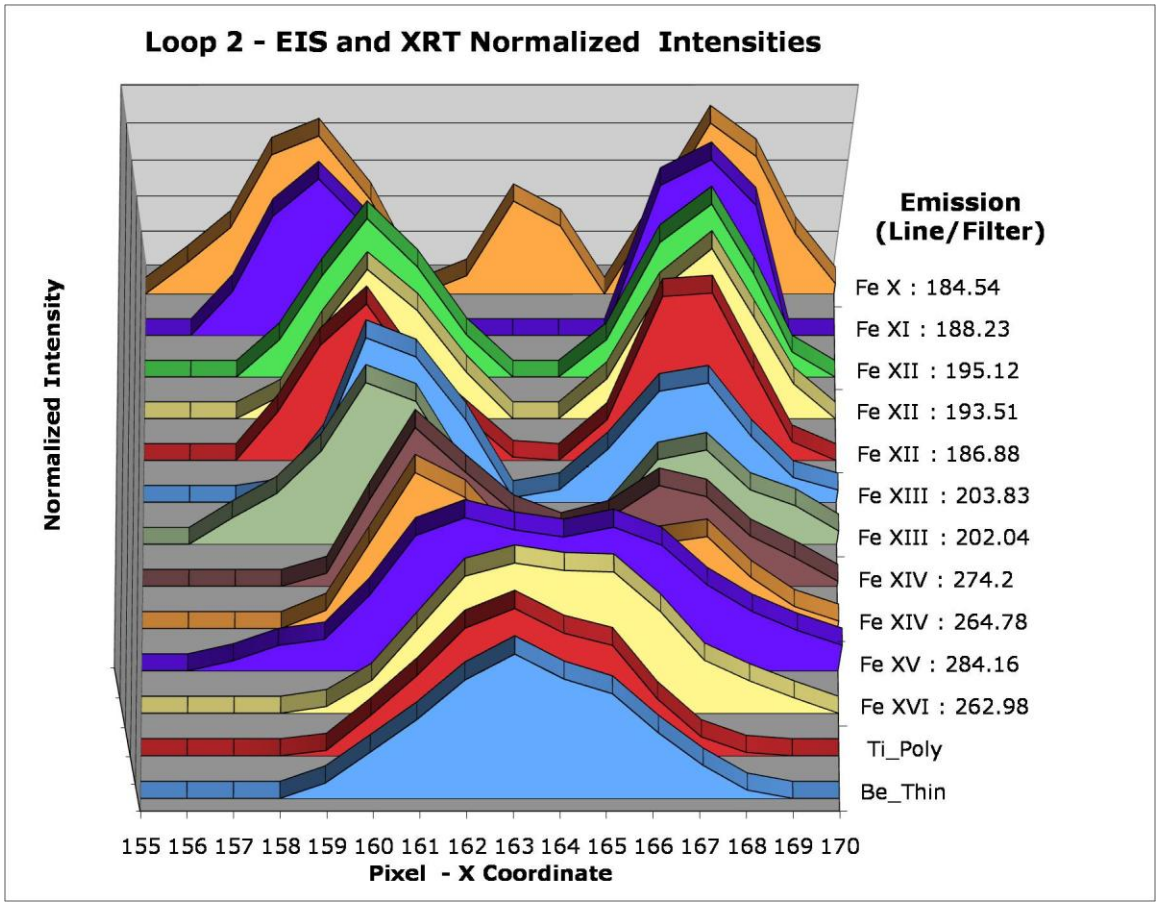

Figure 18: *Loop 2 BG Subtracted Intensities The BG subtracted intensities reveal an underlying loop structure.*

[5] This is the region of the loop was chosen on the basis that it appears the most vertical.

line decreases. This divergent structure does not allow for the standard thermal and density analysis because the choice of any single x coordinate would only include emission from a few lines/filters at a time. To our knowledge, this unusual loop structure has not been observed before, and speculation as to the cause is worthy of exploration.

The first possible explanation to consider is that this highly structured ensemble is a coincidence: i.e. that multiple loops have lined up side by side, in just the right order to produce this type of observation. While hot loops have been observed with cooler loops running parallel, it is highly unlikely that so many loops would line up in parallel with each other in such close proximity. Even more improbable is that the loops would line up in a pattern of hottest loops in the middle with progressively cooler loops bordering each other. Finally, this explanation would also require that the cooler outer loops have nearly the same amount of emission on both sides of the hotter central loops. While this is certainly within the realm of possibilities, it is extremely unlikely that all of these coincidences would occur simultaneously.

A more likely possibility is that this could be an observation of a single thick loop, approximately 15 pixels wide, that is characterized by a hot core with a cooler exterior. If the temperature gradient were large enough, emission might be optically thin when looking directly through each layer, but would become significant when looking through the outer edge of each layer. This is similar the observational effect seen when viewing a planetary nebula or limb darkening. If these types of loops do exist, they may have yet to be observed with any degree of regularity because solar instruments have only just reached the resolution to be able to resolve this type of fine underlying structure. If

this is the case, observations of loops like this should occur with more frequency, particularly as technology continues to improve.

This "fat loop" explanation could be an effect caused by nanoflare storms heating loops consisting of many strands (Klimchuk, submitted). During the course of the storm, individual strands could undergo heating and cooling at different times. If the nanoflare storm were to advance radially inward through the loop, the outer strands would cool before the strands in the core of the loop. To explore this possibility further, a series of XRT observations[6], shown in Figure 19, with the Thin-Al Poly / Ti Poly filters were

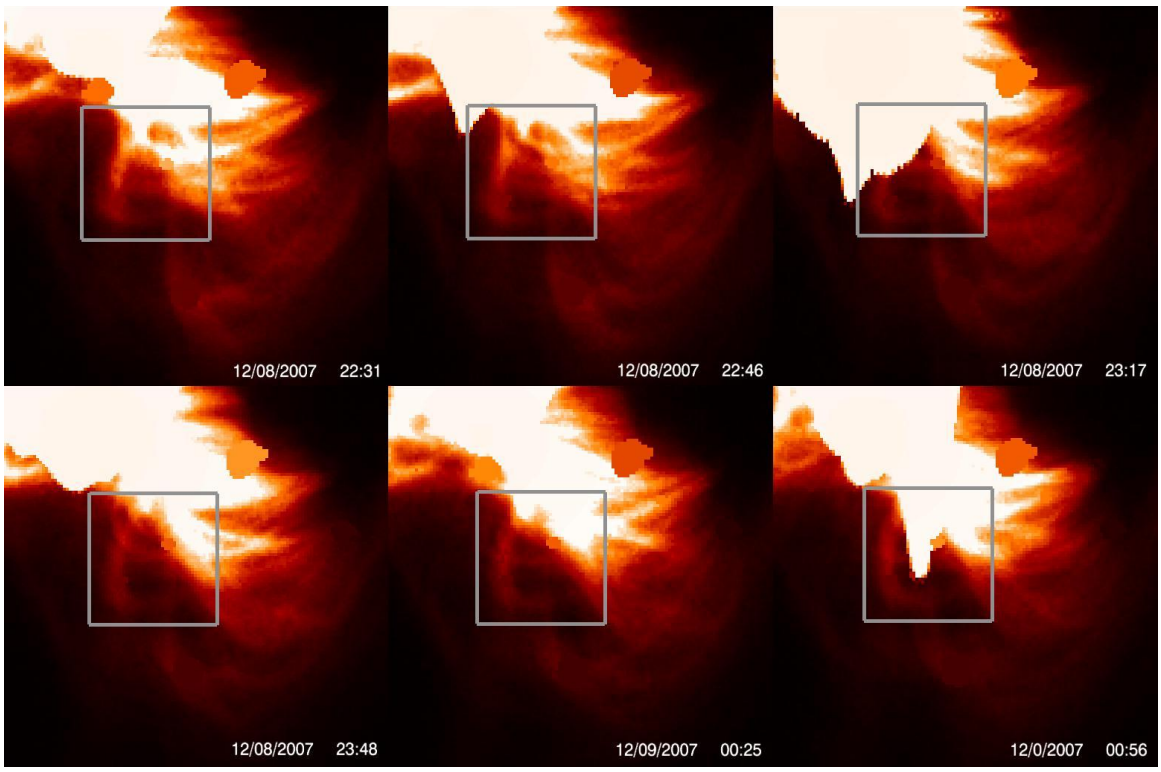

Figure 19: *XRT Time Series. These XRT images, taken with the Thin-Al Poly / Ti Poly filters, provide a time sequence of Loop 2.*

[6] While EIS has better spectral resolution, it took nearly an hour to make the observations used in this analysis. However, XRT is able to an observation in a matter of seconds, offering much better time resolution.

inspected to determine how the loop and AR core evolved over time. These images demonstrate that the nearby AR core is active. While Loop 2 remained relatively stationary during the time sequence, it did undergo some brightening and darkening over the two and a half hour period. This is evidence that heating and cooling of the loop is occurring, suggesting that nanoflare storm activity could explain the observed structure.

While this scenario provides a possible explanation, the available data is insufficient to determine the cause of the structure observed in Loop 2. Ideally, a spectrometer with the spectral and spatial resolution of EIS and time resolution of XRT could provide a time sequence of spectral data that would be able to offer an answer to what is actually occurring. Sadly, such a devise is not currently realistic. However, the next generation solar observatory, SDO, has already been launched and first light is expected sometime around the end of March 2010. The AIA instrument aboard SDO houses four telescopes, each with multiple filters, which will observe the Sun in many wavelengths simultaneously. Able to make an observation in less than 10 seconds, it will produce images with a resolution close to 1 arcsec[7]. With these capabilities, it would be able to provide deeper insight into loops such as Loop 2. Lockheed Martin (http://aia.lmsal.com/) states that "AIA will produce data required for quantitative studies of the evolving coronal magnetic field, and the plasma that it holds, both in quiescent phases and during flares and eruptions."

[7] This is comparable to the spatial resolution of EIS.

4.3. Closing Remarks

Discovering the coronal heating mechanism is a clear example of the arduous journey that a scientist must face in the pursuit of unraveling the mysteries of the universe. Presenting a new idea can be a tedious ordeal. In an ideal world, people would embrace the knowledge being brought before them. However, in order for science to be successful, a system of checks and balances is needed. Controversies arise and at times the burden of proof (especially in the eyes of the scientific community) can be overwhelming, taking years to formulate and requiring many sacrifices – in the extreme cases it has even cost some their lives. This only goes to highlight the importance of scientific debate. As a scientist, one has the responsibility to listen, to learn, and to explore. Careful analysis is required, but let the data speak for itself. In time the answers will come, sometimes when least expected.

"Sit down before fact as a little child, be prepared to give up every preconceived notion, follow humbly wherever and to whatever abysses nature leads, or you shall learn nothing" – T.H. Huxley

REFERENCES

Aschwanden, M. J. 2002, *Astrophysical Journal*, 580, L79

Aschwanden, M. J., Newmark, J. S., Delaboudinie`re, J.-P., Neupert, W. M., Klimchuk, J. A., Gary, G. A., Portier-Fozzani, F., and Zucker, A. 1999, *Astrophysical Journal*, 515, 842

Aschwanden, M. J., and Nightingale, R. W. 2005, *Astrophysical Journal*, 633, 499

Bennett, J., Donahue, M., Schneider, N., and Voit, M. 2004. *The Cosmic Perspective*. Pearson Education, Inc.

Culhane, J.L., et al. 2007, *Solar Physics*, 243, 19

Dere, K. P., Landi, E., Mason, H. E., Monsignori-Fossi, B. C., and Young, P.R. 1997, *Astronomy and Astrophysics Supplement Series*, 125, 149

Fludra, A., and Schmelz, J. T. 1999, *Astronomy and Astrophysics*, 348, 286

Golub, L. and Pasachoff, J.M. 1997. *The Solar Corona*. Cambridge: University Press.

Golub, L. and Pasachoff, J.M. 2001. *Nearest Star*. Harvard University Press.

Golub, L., et al. 2007, *Solar Physics*, 243, 63

Klimchuk, J.A,, Karpen, J. T., and Antiochos, S.K. 2010, *Astrophysical Journal*, submitted

Kosugi, T., et al. 2007, *Solar Physics*, 243, 3

Kutner, M. L. 2003. *Astronomy: A Physical Perspective*. Cambridge: University Press.

Lenz, D. D., DeLuca, E. E., Golub, L., Rosner, R., and Bookbinder, J. A. 1999, *Astrophysical Journal*, 517, L155

Martens, P. C. H., Cirtain, J. W., and Schmelz, J. T. 2002, *Astrophysical Journal*, 577, L115

Mazzotta, P., Mazzitelli, G., Colafrancesco, S., and Vittorio, N. 1998, *Astronomy and Astrophysics Supplement Series*, 133, 403

Pasachoff, J.M. 2000. *Peterson Field Guide: Stars and Planets*. Houghton Mifflin Company.

Phillips, J.H. 1992. *Guide to the Sun*. Cambridge: University Press.

Priest, E. R., Foley, C. R., Heyvaerts, J., Arber, T. D., Culhane, J. L., and Acton, L. W. 1998, *Nature*, 393, 545

Rosner, R., Tucker, W. H., and Vaiana, G. S. 1978, *Astrophysical Journal*, 220, 643

Schmelz, J. T., Scopes, R. T., Cirtain, J. W., Winter, H. D., and Allen, J. D. 2001, *Astrophysical Journal*, 556, 896

Schmelz, J. T. 2002, *Astrophysical Journal*, 578, L161

Schmelz, J. T., Beene, J. E., Nasraoui, K., Blevins, H. T., Martens, P. C. H., and Cirtain, J. W. 2003, *Astrophysical Journal*, 599, 604

Schmelz, J. T., V. L. Kashyp, and M. A. Weber 2007, *Astrophysical Journal*, 660, L157

Schmelz, J. T. and P.C.H. Mertens 2006, *Astrophysical Journal*, 636, L49

Schmelz, J. T., Nasraoui, K., Richardson, V. L., Hubbard, P. J., Nevels, C. R., and Beene, J. E. 2005, *Astrophysical Journal*, 627, L81

Schmelz, J. T., Scott, J., and Rightmire, L.A. 2008, *Astrophysical Journal*, 684, L115

Sparke, L.S. and Gallagher, J.S. 2000. *Galaxies in the Universe: An Introduction*. Cambridge: University Press.

Weber, M. A., Schmelz, J. T., DeLuca, E. E., and Roames, J. K. 2005, *Astrophysical Journal*, 635, L101

The following URLs were also referenced:

Atmospheric Imaging Assembly. http://aia.lmsal.com/

EIS Tutorial. http://solar.bnsc.rl.ac.uk/~young/solarb_eis/paris_tutorial/

Hinode EIS Data Search Form.
http://msslxr.mssl.ucl.ac.uk:8080/SolarB/SearchArchive.jsp

High Altitude Observatory. http://www.hao.ucar.edu/education/spTimeline.php

NASA/Marshall Space Flight Center. The Big Questions.
http://solarscience.msfc.nasa.gov/quests.shtml

SolarSoft. http://www.lmsal.com/solarsoft/

SAO Hinode XRT Search Form. http://kurasuta.cfa.harvard.edu/cgi-bin/VSO/prod/searchForm.pl?time=1&instrument=1&version=current&build=1&provider=SAO&prov_excl=1

XRT SolarSoft Tutorial. http://xrt.cfa.harvard.edu/science/XRT_tutorial_data2.txt

Yohkoh Solar Observatory. http://www.lmsal.com/SXT/main.html